Open access • Journal Article • DOI:10.1088/0004-637X/764/2/176

Widespread and Hidden Active Galactic Nuclei in Star-Forming Galaxies at Redshift > 0.3 — Source link

Stéphanie Juneau, Stéphanie Juneau, Mark Dickinson, Frédéric Bournaud ...+24 more authors

Institutions: University of Arizona, DSM, Durham University, Max Planck Society ...+11 more institutions

Published on: 20 Feb 2013 - The Astrophysical Journal (IOP Publishing)

Topics: Luminous infrared galaxy, Radio galaxy, Quasar, Active galactic nucleus and Galaxy

Widespread and hidden active galactic nuclei in star-forming galaxies at redshift >0.3

Stéphanie Juneau, Mark Dickinson, Frédéric Bournaud, David M. Alexander, Emanuele Daddi, James R. Mullaney, Benjamin Magnelli, Jeyhan S. Kartaltepe, Ho Seong Hwang, S. P. Willner, et al.

To cite this version:

Stéphanie Juneau, Mark Dickinson, Frédéric Bournaud, David M. Alexander, Emanuele Daddi, et al.. Widespread and hidden active galactic nuclei in star-forming galaxies at redshift >0.3. The Astrophysical Journal, American Astronomical Society, 2013, 764, pp.176. 10.1088/0004-637X/764/2/176 . cea-00825844

HAL Id: cea-00825844
https://hal-cea.archives-ouvertes.fr/cea-00825844
Submitted on 30 Jun 2020

The Astrophysical Journal, 764:176 (19pp), 2013 February 20 doi:10.1088/0004-637X/764/2/176

WIDESPREAD AND HIDDEN ACTIVE GALACTIC NUCLEI IN STAR-FORMING GALAXIES AT REDSHIFT >0.3

Stéphanie Juneau[1,2], Mark Dickinson[3], Frédéric Bournaud[1], David M. Alexander[4], Emanuele Daddi[1], James R. Mullaney[4], Benjamin Magnelli[5], Jeyhan S. Kartaltepe[3], Ho Seong Hwang[6], S. P. Willner[6], Alison L. Coil[7], David J. Rosario[8], Jonathan R. Trump[9], Benjamin J. Weiner[2], Christopher N. A. Willmer[2], Michael C. Cooper[10], David Elbaz[1], S. M. Faber[9], David T. Frayer[11], Dale D. Kocevski[9,12], Elise S. Laird[13], Jacqueline A. Monkiewicz[3,14], Kirpal Nandra[8], Jeffrey A. Newman[15], Samir Salim[16], and Myrto Symeonidis[17]
[1] CEA-Saclay, DSM/IRFU/SAp, F-91191 Gif-sur-Yvette, France; stephanie.juneau@cea.fr
[2] Steward Observatory, University of Arizona, Tucson, AZ 85721, USA
[3] National Optical Astronomy Observatory, 950 North Cherry Avenue, Tucson, AZ 85719, USA
[4] Department of Physics, Durham University, Durham DH1 3LE, UK
[5] Max-Planck-Institüt für extraterrestrische Physik, Postfach 1312, D-85741 Garching bei München, Germany
[6] Harvard-Smithsonian Center for Astrophysics, 60 Garden Street, Cambridge, MA 02138, USA
[7] Department of Physics, Center for Astrophysics and Space Sciences, University of California, 9500 Gilman Dr., La Jolla, San Diego, CA 92093, USA
[8] Max-Planck-Institüt für extraterrestrische Physik, Giessenbachstrasse, D-85748 Garching bei München, Germany
[9] University of California Observatories/Lick Observatory, University of California, Santa Cruz, CA 95064, USA
[10] Center for Galaxy Evolution, Department of Physics and Astronomy, University of California-Irvine, 4129 Frederick Reines Hall, Irvine, CA 92697, USA
[11] National Radio Astronomy Observatory, P.O. Box 2, Green Bank, WV 24944, USA
[12] Department of Physics and Astronomy, University of Kentucky, Lexington, KY 40506-0055, USA
[13] Astrophysics Group, Imperial College London, Blackett Laboratory, Prince Consort Road, London SW7 2AZ, UK
[14] School of Earth and Space Exploration, Arizona State University, Tempe, AZ 85287, USA
[15] Department of Physics and Astronomy, University of Pittsburgh, 401-C Allen Hall, 3941 O'Hara Street, Pittsburgh, PA 15260, USA
[16] Department of Astronomy, Indiana University, Bloomington, IN 47404, USA
[17] University College London, Mullard Space Science Laboratory, Surrey RH5 6NT, UK
Received 2012 September 18; accepted 2013 January 7; published 2013 February 5

ABSTRACT

We characterize the incidence of active galactic nuclei (AGNs) in $0.3 < z < 1$ star-forming galaxies by applying multi-wavelength AGN diagnostics (X-ray, optical, mid-infrared, radio) to a sample of galaxies selected at 70 μm from the Far-Infrared Deep Extragalactic Legacy survey (FIDEL). Given the depth of FIDEL, we detect "normal" galaxies on the *specific star formation rate* (sSFR) *sequence* as well as starbursting systems with elevated sSFR. We find an overall high occurrence of AGN of 37% ± 3%, more than twice as high as in previous studies of galaxies with comparable infrared luminosities and redshifts but in good agreement with the AGN fraction of nearby ($0.05 < z < 0.1$) galaxies of similar infrared luminosities. The more complete census of AGNs comes from using the recently developed Mass-Excitation (MEx) diagnostic diagram. This optical diagnostic is also sensitive to X-ray weak AGNs and X-ray absorbed AGNs, and reveals that absorbed active nuclei reside almost exclusively in infrared-luminous hosts. The fraction of galaxies hosting an AGN appears to be independent of sSFR and remains elevated both on the sSFR sequence and above. In contrast, the fraction of AGNs that are X-ray absorbed increases substantially with increasing sSFR, possibly due to an increased gas fraction and/or gas density in the host galaxies.

Key words: galaxies: active – galaxies: evolution – galaxies: high-redshift – galaxies: ISM – galaxies: star formation – infrared: galaxies

Online-only material: color figures

1. INTRODUCTION

It has become increasingly clear that we need to reconcile the formation of stars in galaxies with the growth of the supermassive black holes (SMBHs) at their centers for a complete picture of galaxy evolution. Theoretically, active galactic nuclei (AGNs) are invoked as a means to quench star formation in galaxies thereby explaining the presence of massive red galaxies at recent epoch. Without this so-called AGN feedback, both semi-analytic models and cosmological simulations tend to overproduce massive blue galaxies (e.g., Croton et al. 2006; Gabor et al. 2011). Together with the tight relation between SMBH mass and bulge mass (Magorrian et al. 1998; Ferrarese & Merritt 2000; Tremaine et al. 2002), this leads to a picture of co-evolution between galaxy stellar content and central SMBH (but see Jahnke & Macciò 2011 for an alternative interpretation). However, observational evidence of a physical connection between star formation and AGN remains sparse and mostly indirect, especially during the growth phase (pre-quenching).

Different triggers of SMBH growth have been proposed: major galaxy mergers (Sanders et al. 1988; Di Matteo et al. 2005; Hopkins et al. 2006), large-scale disk instabilities (Bournaud et al. 2011), and a secular growth where SMBH growth is unrelated to the star formation rate (SFR) of galaxies (Shao et al. 2010; Cisternas et al. 2011; Mullaney et al. 2012). Some of these studies favor hybrid models where the high-luminosity end (quasar regime, with $L_{\rm AGN} > 10^{44}$ erg s^{-1}) is dictated by major galaxy mergers while the lower-luminosity AGNs follow a secular evolution (e.g., Shao et al. 2010; Lutz et al. 2010; Rosario et al. 2012). However, the role of AGNs and their underlying physical connection with host galaxies remain uncertain. Most studies of the host galaxy morphologies of high-redshift (>0.5) AGNs, which have tried to distinguish the relative importance of major merger and secular growth, have relied on X-ray-selected samples of AGN (Gabor et al.

2009; Cisternas et al. 2011; Schawinski et al. 2011; Kocevski et al. 2012). The main drawback of this approach as a test of the major merger hypothesis is the potential insensitivity to a key phase of AGN growth—when the SMBH is expected to be deeply buried in the gas-rich center of the merging system (Sanders et al. 1988). During that buried phase, X-ray emission from the AGN may be mostly absorbed by intervening material with high column densities and thus may be undetected in even the deepest X-ray surveys currently available. Thus, a real test of this connection and of the AGN content of actively star-forming (SF) galaxies requires the identification of both absorbed and unabsorbed AGNs.

Nebular emission lines tracing the narrow-line regions (NLRs) surrounding AGNs are not subject to the same small-scale obscuration as X-rays owing to their much larger physical extent (hundreds of pc to a few kpc scales). Indeed, the [O III] λ5007 luminosity combined with hard (2–10 keV) X-ray luminosity has been used as a Compton-thickness parameter in order to infer the X-ray absorption (Mulchaey et al. 1994; Bassani et al. 1999; Heckman et al. 2005; Juneau et al. 2011, hereafter J11; also see the Appendix). AGNs identified at visible wavelengths tend to either have a direct view of the nuclear region with low-level obscuration by dust in the host galaxy (Type 1 AGNs, recognized by broad emission lines) or a large obscuration of the nuclear region along the line of sight combined with a lesser obscuration of the NLRs (Type 2 AGNs, lacking broad emission lines[18]).

In extreme cases where both X-ray emission and optical line emission are completely obscured, infrared light may reveal an AGN by showing reprocessed thermal emission from AGN-heated dust grains. Compared to the bulk of stellar light, the more energetic radiation field from an AGN heats the dust to higher temperatures, adding a hot dust component with thermal emission at shorter MIR wavelengths (Elvis et al. 1994; Lacy et al. 2004; Stern et al. 2005; Mullaney et al. 2011). This extra hot dust alters the mid-IR spectral energy distribution (SED) by producing an excess between the usual stellar bump at $\sim 1.6\,\mu$m and the stellar-heated dust emission at $>10\,\mu$m. Broadband MIR observations such as those from *Spitzer*/IRAC can probe that feature (Lacy et al. 2004; Stern et al. 2005; Donley et al. 2007, 2012). Not all AGNs will exhibit MIR signatures because of the required geometry and dust content. Also, intrinsically weaker AGNs occurring alongside star formation tend not to dominate the IR SED of their host galaxies (Barmby et al. 2006).

Overall, it is clear that no single diagnostic can achieve a complete census of AGNs for all galaxies. As such, combining selections at multiple wavelengths may be the key to achieving both a better sampling and a better understanding of AGNs and their connection with star formation activity.

In this paper, we characterize the incidence of AGN in SF galaxies at intermediate redshift ($0.3 < z < 1$). The multi-wavelength data set and galaxy samples are described in Sections 2 and 3, respectively. The AGN diagnostics are introduced in Section 4. Section 5 contains the results regarding the AGN fraction among SF FIR-selected galaxies (Section 5.1); the occurrence of active nuclei as a function of infrared luminosity (Section 5.3) and as a function of specific star formation rate (sSFR; Section 5.4); the absorption of AGN in relation to host galaxies (Section 5.5); and the influence of AGN emission on mid- to far-infrared color, probing the dust temperature on the warm side of the infrared SED (Section 5.6). The caveats are discussed in Section 6.1, followed by the possible connections between AGN obscuration and host galaxies (Section 6.2), the properties of the AGNs selected via different wavelength regimes (Section 6.3), and possible physical interpretations of the triggering mechanisms of AGN in Section 6.4. Lastly, we summarize our findings in Section 7. We assume a flat cosmology with $\Omega_m = 0.3$, $\Omega_\Lambda = 0.7$, and $h = 0.7$ throughout, and a Chabrier (2003) initial mass function (IMF) when deriving stellar masses and SFRs.

2. MULTI-WAVELENGTH DATA SET

The primary intermediate-redshift galaxy sample is based on observations from the Great Observatories Origins Deep Survey[19] (GOODS) and the All-wavelength Extended Groth strip International Survey[20] (AEGIS), specifically in the GOODS-North and the Extended Groth Strip (EGS) fields.

2.1. Infrared Photometry

Both fields were observed during the Far-Infrared Deep Extragalactic Legacy survey (FIDEL; Dickinson & FIDEL team 2007), yielding sensitive *Spitzer* observations at $24\,\mu$m and $70\,\mu$m (respective 3σ limiting fluxes of $\sim 20\,\mu$Jy and 2.5 mJy). MIPS photometry was obtained using a guided extraction method, where images at shorter wavelength, less subject to confusion, are used to build a set of prior positions to fit for the same sources at longer wavelengths. In this case, Infrared Array Camera (IRAC) $3.6\,\mu$m images were used to select priors which were then fit simultaneously at $24\,\mu$m. Next, sources with a $24\,\mu$m detection were fit at $70\,\mu$m. The data and method are described in more detail by Magnelli et al. (2009, 2011). Using Monte Carlo simulations, these authors found that this method can deblend sources that are at least $0.5 \times$ FWHM apart ($\sim 9''$ for MIPS $70\,\mu$m), and they quantified the systematic uncertainties using the difference between the extracted flux of simulated sources to the real input flux (Magnelli et al. 2009). The latest catalogs in GOODS (Magnelli et al. 2011) include two estimates of the uncertainties: the systematic uncertainties quantified from the Monte Carlo simulations, as well as local background noise uncertainties (from the residual maps). We use the maximum of the two values for each galaxy.

Spitzer/IRAC photometry is available in all four channels (3.6, 4.5, 5.8, and $8.0\,\mu$m; available through the Spitzer Science Center for GOODS-N and from Barmby et al. 2008 for EGS). In what follows, IRAC photometry is used to calculate rest-frame *K*-band magnitudes, which are in turn used to estimate stellar masses when the latter are not available through SED fitting. In addition, IRAC photometry is used for mid-infrared color–color AGN diagnostics (Section 4.3).

2.2. Optical Spectra

As in the work by J11, the GOODS-N optical spectra are drawn from the Team Keck Redshift Survey[21] (TKRS; Wirth et al. 2004), whereas the EGS spectra come from the DEEP2 Galaxy Redshift Survey (hereafter DEEP2; Davis et al. 2003, 2007; Newman et al. 2012). However, we augment the sample with spectra obtained during the DEEP3 campaign including

---

[18] Additionally, some Type 2 (narrow lines only) AGNs may be radiatively inefficient and simply lack broad-line regions (e.g., Trump et al. 2011) but these systems are intrinsically weaker and presumably have less effect on their host galaxies.

[19] http://www.stsci.edu/science/goods/

[20] http://aegis.ucolick.org/

[21] http://tkserver.keck.hawaii.edu/tksurvey/

galaxies in GOODS-N (Cooper et al. 2011) and EGS (Cooper et al. 2012; M. C. Cooper et al., in preparation).

All sets of observations were obtained with Keck/DEIMOS and reduced with the same pipeline[22] (Cooper et al. 2012; Newman et al. 2012). However, their spectral resolution and spectral range differ due to the use of different gratings (600 line mm^{-1} for TKRS and DEEP3, and 1200 line mm^{-1} for DEEP2). The TKRS and DEEP3 resolution is 4 Å FWHM over the wavelength range 5500–9800 Å, whereas DEEP2 spectra have a resolution of 2 Å FWHM with a wavelength coverage of 6500–9100 Å.

Emission-line fluxes are measured as described in J11, by fitting a Gaussian curve to each line individually and integrating the flux over $\pm 2.5\sigma$, where σ is the Gaussian width (=FWHM/2.355). Through this paper, we are only concerned with the Hβ/[O III] λ5007 flux ratio and with the [O III] λ5007 luminosity. The Hβ fluxes are corrected for underlying Balmer absorption either by using a population synthesis model fit to the continuum (with Bruzual & Charlot 2003 models when the median S/N per pixel is greater than 3), or by applying the median equivalent width of 2.8 ± 0.9 Å found in J11 to correct for Balmer absorption for spectra with low S/N.

2.3. X-Ray Data

We take advantage of the fact that the *Chandra* X-ray coverage is very deep: 2 Ms in GOODS-N (Alexander et al. 2003), 200 ks (Laird et al. 2009; Nandra et al. 2005), and 800 ks in the EGS (E. S. Laird et al., in preparation; reduced in a similar fashion as Laird et al. 2009). In the EGS, we favor the 800 ks X-ray fluxes when available, and use the wider area 200 ks observations otherwise. The shallower EGS X-ray data (200 ks) are sufficient to detect moderate luminosity X-ray AGNs ($L_{2\text{–}10\,\mathrm{keV}} > 10^{42}\,\mathrm{erg\,s^{-1}}$) out to $z \sim 1$. Furthermore, we can detect fainter X-ray galaxies (mostly starbursts) in GOODS-N and in the 800 ks portion of the EGS.

X-ray observations are primarily used for AGN identification (Section 4.1). Furthermore, they are used to infer X-ray absorption by comparing the hard X-ray luminosity ($L_{2\text{–}10\,\mathrm{keV}}$, calculated as in J11) to the [O III] λ5007 NLR luminosity ($L_{\mathrm{[O\,III]}}$), a more isotropic tracer of the intrinsic AGN luminosity than X-rays. For that purpose, we derive X-ray upper limits for [O III]-selected AGNs. Upper limits were derived as described by Alexander et al. (2003) in the GOODS-N field, and estimated from the sensitivity maps in the EGS as described by J11.

2.4. AGN Bolometric Luminosity

AGN bolometric luminosities are estimated using $L_{\mathrm{bol}}(\mathrm{AGN}) = 10^3 \times L_{\mathrm{[O\,III]}}$. The bolometric conversion factor to $L_{2\text{–}10\,\mathrm{keV}}$ has been calculated to range from 10 to 70 depending on Eddington ratio and/or X-ray luminosity (Vasudevan & Fabian 2007, 2009). Here we assume $L_{\mathrm{bol}}(\mathrm{AGN}) = 25 \times L_{2\text{–}10\,\mathrm{keV}}$ and another factor of 40 to convert from [O III] to unabsorbed X-ray (2–10 keV) luminosity (the value found by Heckman et al. 2005 for unobscured AGNs).

The AGN bolometric luminosities can be converted to a black hole (BH) mass accretion rate with the following equation (Equation (1) from Alexander & Hickox 2012):

$$\dot{M}_{\mathrm{BH}}[M_\odot\,\mathrm{yr}^{-1}] = 0.15 \left(\frac{0.1}{\epsilon}\right) \left(\frac{L_{\mathrm{bol}}}{10^{45}\,\mathrm{erg\,s^{-1}}}\right), \qquad (1)$$

where ϵ is the efficiency of conversion of mass into energy. We assume a value $\epsilon = 0.1$ in our calculations (Marconi et al. 2004; Merloni 2004).

2.5. Infrared Luminosity and Star Formation Rates

Total infrared luminosities ($8 < \lambda < 1000\,\mu$m) were obtained by fitting the 70 μm flux density and redshift with templates from Chary & Elbaz (2001, hereafter CE01). Even when used with only data at much shorter wavelengths (e.g., MIPS 24 μm) than the peak of typical infrared SEDs (∼60–100 μm), these templates have been shown to give consistent results with direct integration over the longer wavelength *Herschel* bands that probe the peak of the FIR SED in galaxies (out to $z \sim 1.5$; Elbaz et al. 2010).

Because we are interested in the IR luminosity originating from star formation only, observations at 24 μm or shorter wavelengths were not included in the fit. Relative to 70 μm, they are at risk for greater contamination from AGN-heated dust when galaxy nuclei are active (see Section 6.1). Using a contaminated 24 μm measurement would lead to an overestimate of the IR luminosity due to stellar heated dust and of the SFR. It is possible that even observations at 70 μm have an AGN contribution but the effect will be less important than at shorter wavelengths.

Total infrared luminosities were converted to SFRs using the relation from Kennicutt (1998) with an additional conversion factor of 0.66 from a Salpeter (1955) to a Chabrier (2003) IMF.

3. GALAXY SAMPLES

3.1. Intermediate-redshift Samples

We start from a parent sample of spectroscopically selected galaxies at $z > 0.3$ with a spectral coverage that includes the expected wavelengths of the Hβ and [O III] λ5007 emission lines. The resulting redshift range is approximately[23] $0.3 < z < 1$. We will refer to this parent sample of 9435 galaxies as the Inter/All sample (where Inter stands for intermediate redshift).

The Inter/FIR subsample is further defined to have a MIPS 70 μm detection with S/N > 3, yielding a sample of 270 galaxies at $0.3 < z < 1$ (58 in GOODS-N; 212 in EGS). Galaxies in the Inter/FIR sample all have a robust 24 μm detection (S/N > 8) given the much greater sensitivity of the 24 μm observations relative to the 70 μm ones. The Inter/FIR sample includes 94% of MIPS 70 galaxies with a spectroscopic redshift $0.3 < z < 0.8$. This percentage decreases to 82% over the redshift range $0.3 < z < 1$ because the limited spectral range of the DEEP2 setup prevents the coverage of the Hβ and [O III] lines beyond $z > 0.8$.

Among the Inter/FIR sample, 145 (54%) galaxies have valid emission-line measurements with a 3σ detection for both the Hβ and [O III] λ5007 lines, while 62 (23%) galaxies have one detection and one upper limit. This results in 207 (77%) galaxies with a constraint on their [O III] λ5007/Hβ flux ratios. The remaining galaxies have S/N < 3 for both emission lines.

Given the sensitivity of the FIDEL survey at 70 μm, the majority (71%) of the 70 μm selected galaxies at $0.3 < z < 1$ are luminous IR galaxies (LIRGs; with $L_{\mathrm{IR}}(8\text{–}1000\,\mu\mathrm{m}) > 10^{11}\,L_\odot$), as shown in Figure 1. These objects are responsible for a large fraction of the global SFR density at $z \sim 1$ (Le Floc'h et al. 2005; Magnelli et al. 2009) and extend down to the typical

---

[22] http://deep.berkeley.edu/spec2d/, developed by the DEEP2 team at the University of California-Berkeley.

[23] In detail, there is some variation in the wavelength range of individual spectra due to the instrumental setup (as described in Section 2.2) and due to the exact position of the slits on the mask.

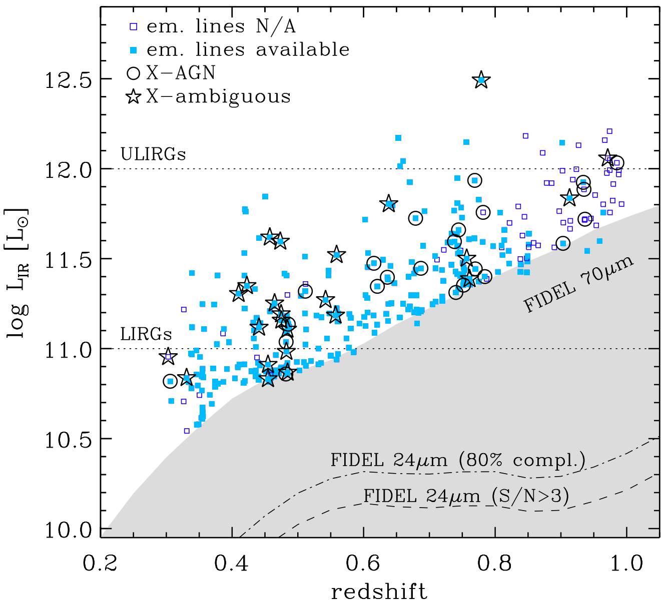

Figure 1. Total infrared luminosity as a function of redshift for 70 μm detected galaxies in GOODS-N and the EGS (all symbols). Galaxies with spectral coverage of both the $H\beta$ and [O III] $\lambda 5007$ emission lines are shown with filled squares (Inter/FIR sample), and the galaxies lacking coverage are shown with open squares. These features shift beyond the wavelength range of DEEP2 spectra by $z \sim 0.8$, explaining the smaller fraction of galaxies with available emission lines at $0.8 < z < 1$. The X-ray classification indicates robust X-ray AGNs (open circles) and X-ray ambiguous cases (open star symbols) with faint *and* soft X-ray emission like X-ray starbursts. We show the 3σ sensitivity limit of the FIDEL survey at 70 μm with the shaded area and the 3σ limit and 80% completeness limit of the 24 μm data (dashed and dot-dashed lines, respectively). All the limits were derived with the CE01 templates.

(A color version of this figure is available in the online journal.)

SF galaxies on the *main sequence* of star formation (Noeske et al. 2007; Elbaz et al. 2007, 2011). Thus, they comprise not only highly starbursting systems, which are thought to only contribute ∼10% of the global star formation rate density (SFRD; Rodighiero et al. 2011; Sargent et al. 2012), but also more representative galaxies that contribute to the remaining 90% of the SFRD.

3.2. Low-redshift Comparison Sample

We build a $z \sim 0$ comparison FIR-selected sample from the Sloan Digital Sky Survey (SDSS) DR7 (Abazajian et al. 2009) based on the detection in the IRAS 60 μm or AKARI 90 μm bands as described by Hwang et al. (2010a, 2010b). Following the procedure in J11, we further select galaxies to be at redshift $0.05 < z < 0.1$ and to have emission-line detections with $S/N > 3$ for all features used in the spectral classification from J11 ($H\beta$, [O III] $\lambda 5007$, $H\alpha$, [N II] $\lambda 6584$, and [S II] $\lambda\lambda 6717, 6731$) yielding a sample of 4034 galaxies, which we call the Low/FIR sample.[24]

The emission-line fluxes were obtained from the Value Added Catalogs developed by the Max-Planck Institute for Astronomy (Garching) and John Hopkins University (MPA/JHU).[25] The methodology for measurements of emission-line fluxes is described by Tremonti et al. (2004). We adopt the AGN classification based on the BPT [N II]- and [S II]-diagrams as described by J11, but using the classification scheme from Kewley et al. (2006) does not alter our results.

4. MULTI-WAVELENGTH AGN DIAGNOSTICS

4.1. X-Ray Diagnostic

The X-ray identification of AGNs is based on two criteria: (1) hard X-ray luminosity $L_{2\text{–}10\,\mathrm{keV}} > 10^{42}\ \mathrm{erg\,s^{-1}}$ or (2) hardness ratio[26] $\mathrm{HR} > -0.1$, corresponding to an effective photon index $\Gamma < 1$. These conditions are similar to the X-ray criteria employed by Bauer et al. (2004) based on observed trends that nearby galaxies without AGN do not exceed a luminosity of $3 \times 10^{42}\ \mathrm{erg\,s^{-1}}$ in the 0.5–8 keV band (e.g., Fabbiano 1989), and that X-ray sources of stellar origin are characterized by comparatively soft X-ray emission with photon indices $\Gamma > 1$ (Colbert et al. 2004; see also Figure 2 of Alexander et al. 2005).

The 2–10 keV rest-frame luminosities were computed using k-correction as described by J11 but not corrected for intrinsic absorption within the galaxies. Several other studies also adopt such a luminosity threshold when selecting samples of AGNs from deep X-ray surveys (e.g., Cisternas et al. 2011; Schawinski et al. 2011; Mullaney et al. 2012). The addition of a hardness criterion in the current study allows us to include weaker and/or more absorbed AGN, although only 1 among 19 X-ray AGNs has $L_{2\text{–}10\,\mathrm{keV}} < 10^{42}\ \mathrm{erg\,s^{-1}}$.

X-ray-detected sources that do not fulfill the AGN criteria are considered "X-ray ambiguous," as the X-ray emission could have a stellar origin rather than being due to AGN activity. However, a faint and soft X-ray emission can also be present in extremely absorbed AGNs if, for instance, there is a concurrent X-ray starburst or if the X-ray spectrum is reflection-dominated rather than transmission-dominated. Nearby Compton-thick AGNs are observed to span a broad range of spectral indices (see Figure 11 of Juneau et al. 2011).

4.2. MEx Diagnostic Diagram

The second AGN identification method is the Mass-Excitation (MEx) diagnostic diagram introduced by J11. The MEx diagram plots stellar mass versus the [O III] $\lambda 5007/H\beta$ flux ratio (Figure 2(a)). Empirical dividing lines indicate spectrally distinct regions of the MEx diagram: optically identified AGNs tend to lie above the lines, purely SF galaxies below the lines, and the MEx-intermediate region (between the lines) contains a sharp transition from SF to AGN galaxies as indicated by the strong gradient from $P(\mathrm{AGN}) = 0\%$ to $P(\mathrm{AGN}) = 100\%$. While we use the dividing lines for discussion and visualization, the analysis relies more importantly on the AGN probability values.[27] Those probabilities are determined by using a set of priors from the SDSS as described by J11 and correspond, for a given observed galaxy, to the fraction of AGNs of any type (Seyfert 2, composite, LINER) relative to the total number of galaxies located within the measured uncertainties on the [O III] $\lambda 5007/H\beta$–M_* plane.

The main strengths of the MEx diagram are its applicability to higher redshift relative to traditional BPT diagrams[28] and

---

[24] The S/N requirement was relaxed for galaxies with SDSS flag *spclass* = 3 in order to retrieve broad-line AGNs. Among 64 *spclass* = 3 objects (1.5% of Low/FIR sample), 40 have $S/N > 3$ in the catalog and the remaining 24 either had a lower S/N or were not measured in the MPA/JHU catalog due to the breadth of the lines ($>700\ \mathrm{km\,s^{-1}}$).

[25] Available for DR7: http://www.mpa-garching.mpg.de/SDSS/DR7/

[26] Hardness Ratio $\equiv (H - S)/(H + S)$, where H and S are the X-ray count rates in the hard (2–8 keV) and soft (0.5–2 keV) bands, respectively.

[27] See https://sites.google.com/site/agndiagnostics/home/mex for software to compute the MEx-AGN classification.

[28] BPT diagrams require $H\alpha$ and other fairly red emission lines ([N II] $\lambda 6584$, [S II] $\lambda\lambda 6717, 6731$, or [O I] $\lambda 6300$), which redshift out of the visible window at $z > 0.4$.

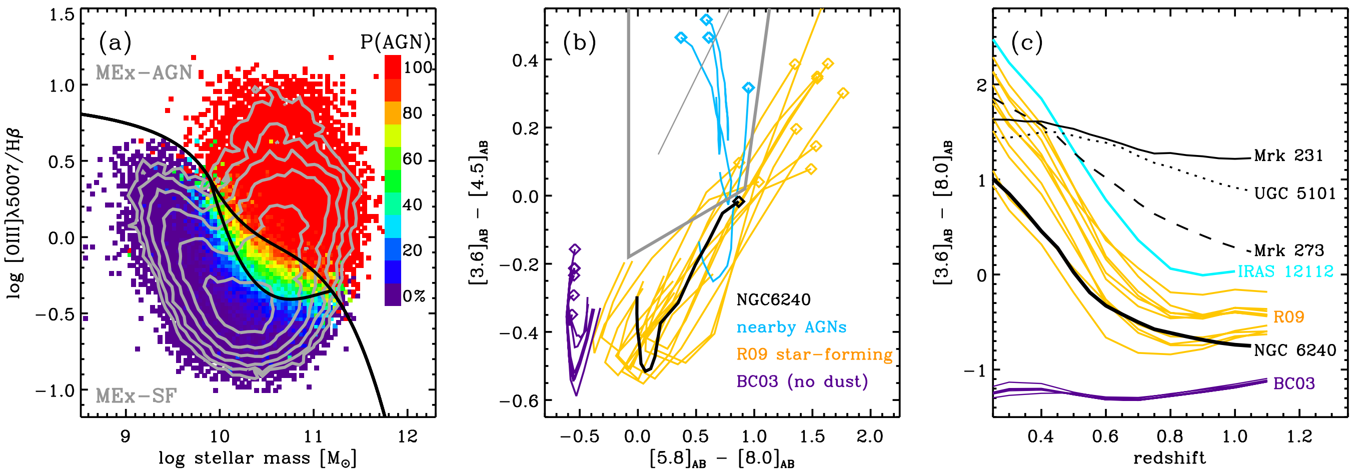

Figure 2. AGN diagnostic diagrams: (a) the MEx introduced in J11. The empirical curves (solid lines) split the diagrams into galaxy spectral types as labeled, with a MEx-intermediate region between the MEx-AGN and MEx-SF classes. The logarithmic contours show the number density of the SDSS galaxy sample used to define AGN probabilities (color bar). (b) IRAC color–color diagram from Stern et al. (2005). The AGN selection box (thick solid line) and the power-law locus (thin solid line) are marked in gray. IRAC colors are computed for various templates as a function of redshift from $z = 0.3$ (open diamonds) to $z = 1$. Namely, we display the expected colors of nearby star-forming LIRGs and ULIRGs from the templates from Rieke et al. (2009, in yellow), nearby AGNs in light blue, dust-free stellar population models using BC03 templates in purple, and we highlight a nearby Compton-thick double AGN, NGC 6240, with a thick black line. (c) IRAC color between observed channels 1 and 4 as a function of redshift. The cyan curve, which corresponds to the redshift track of IRAS 12112+0305, is the star-forming galaxy template showing the most extreme IRAC colors. The remainder of the star-forming galaxy templates from Rieke et al. (2009, yellow tracks) span a fairly restricted range in color. Galaxies above that range are suspected to host AGN activity. This picture is supported by the projected colors of a few nearby AGNs (black lines: Mrk 231 (solid); UGC 5101 (dotted line); and Mrk 273 (dashed line); but also see Compton-thick AGN NGC 6240 (thick solid)). The dust-free stellar population models from BC03 define the lower envelope (purple tracks).

(A color version of this figure is available in the online journal.)

the use of a probabilistic approach to assess the reliability of a given spectral class. In the remainder of this work, we use the AGN probability $P(\mathrm{AGN})$ to count the number of AGNs (e.g., a galaxy with $P(\mathrm{AGN}) = 30\%$ is counted as 0.3 AGN instead of 1 AGN) in cases where an AGN is identified only with the MEx method. The AGN fraction is defined as follows:

$$\text{AGN fraction} = \frac{1}{N}\sum_{i=1}^{N} P(\mathrm{AGN})_i , \qquad (2)$$

where the AGN probability $P(\mathrm{AGN})$ varies from 0 to 1 and is summed over the number of galaxies N that belong to the subsample of interest. This approach reduces the risk of contamination by SF galaxies into the AGN samples but may lead to underestimating the total AGN fraction as composite galaxies, which mostly harbor AGNs (e.g., Trouille et al. 2011), tend to have $P(\mathrm{AGN}) < 100\%$. The initial values of $P(\mathrm{AGN})$ are obtained from the MEx diagnostic ($P_{\mathrm{MEx}}(\mathrm{AGN})$). However, AGNs identified from an alternative method (X-ray or IR colors) are set to have $P(\mathrm{AGN}) = 1$. The 68.3% confidence intervals on fractions are determined with Bayesian binomial statistics following the formalism and IDL[29] implementation of Cameron (2011).

The MEx diagnostic diagram successfully detects AGNs that are missed in even the deepest X-ray surveys. J11 showed that at least some of the X-ray undetected galaxies with a probability >30% of hosting an AGN contain X-ray absorbed AGN activity. Indeed, X-ray stacks revealed detections in both the soft and hard bands of the *Chandra* X-ray observations with a flat spectral slope indicating X-ray absorption. Although the MEx-AGN classification may not always hold on an individual galaxy basis, it was validated overall to $z = 1$ for average galaxy populations (Juneau et al. 2011), and preliminary studies at slightly higher redshifts suggest that the MEx method remains valid on average ($z \sim 1.5$; Trump et al. 2013). Furthermore, Mullaney et al. (2012) found that the mean stellar mass of X-ray-selected AGN hosts did not evolve between $0.5 < z < 3$. This trend suggests that the diagnostic power of the MEx diagram may hold at those higher redshifts for the moderate to luminous AGNs ($L_{\mathrm{bol}} > 10^{43.4}$ erg s^{-1}). Nevertheless, we limit the analysis to $z < 1$ in this work, where the MEx diagnostic can be applied with a high level of confidence.

4.3. IRAC Single-color and Two-color Diagnostics

Infrared AGN identification methods rely on probing AGN-heated dust. Lacy et al. (2004) and Stern et al. (2005) reported that combinations of IRAC colors select both obscured and unobscured luminous AGNs. These studies were based on fairly shallow IRAC data. Barmby et al. (2006) found that the Lacy and Stern MIR diagnostics, when applied to more sensitive IRAC data, miss a significant fraction of X-ray-selected AGNs and suffer from more contamination from non-AGN galaxies. The latter is caused by the deeper observations probing to higher redshift ($z > 1$) and making the IRAC colors of starburst and normal SF galaxies appear redder and moving into the AGN selection box (Donley et al. 2007).

Here, we adopt the IRAC color–color diagram developed by Stern et al. (2005) because it was shown to suffer from less SF galaxy contamination than the Lacy diagram when applied to higher-redshift and to more sensitive IRAC observations (Donley et al. 2007). The diagram is shown in Figure 2(b), where AGNs nominally lie in the upper boxed region. We show some tracks of expected mid-infrared colors for various galaxy templates. We do not expect strong contamination by SF galaxies at $z < 1$, but some well-known AGNs are located outside of the AGN region when their colors are redshifted.

Because IRAC color–color diagrams do not include information about the redshift of the galaxies, there are degeneracies

---

[29] Interactive Data Language.

in observed colors from overlapping redshift tracks of different galaxy populations (see, e.g., Donley et al. 2007, 2012). To remove such degeneracies, we use the IRAC [3.6]–[8.0] color as a function of redshift. As shown in Figure 2(c), infrared-selected SF galaxies occupy a distinct region from nearby AGN,[30] especially at $z > 0.5$. The outermost SF galaxy template is for IRAS 12112+0305, which we use to separate the IRAC SF galaxies (below the cyan curve) from the IRAC AGN candidates (above the cyan curve). The change in IRAC [3.6]–[8.0] color with redshift of the infrared-selected SF galaxies is due in part to the aromatic features at rest-frame wavelengths 6.2–8.6 μm gradually shifting outside of the [8.0] band (between $0 < z < 0.4$) and the stellar bump at rest-frame $\sim$1.6 μm entering the [3.6] band at $0.7 < z < 1.2$. When AGN-heated dust dominates the mid-IR emission, the near power-law shape of the continuum causes a flatter [3.6]–[8.0] change of color with redshift, as exemplified by Mrk 231 and UGC 5101. Lastly, dust-free stellar population templates (Bruzual & Charlot 2003) set a lower envelope to the observations. When galaxies are nearly or completely dust-free, the IRAC color corresponds to that of stellar photospheres.

4.4. Radio AGN Diagnostic

Radio-excess AGNs can be identified by an excess of radio emission relative to the FIR–radio correlation (e.g., Roy & Norris 1997; Donley et al. 2005; Del Moro et al. 2013), which otherwise is very tight for SF galaxies and many radio-quiet AGNs (see review by Condon 1992). Radio AGN identification was found to reveal a different AGN population with limited overlap with the X-ray and IRAC color AGN diagnostics (Hickox et al. 2009). However, radio AGNs were also found to reside in different host galaxies, characterized with, on average, higher stellar masses, stronger clustering, and passive stellar activity compared to the hosts of X-ray or IR AGNs (Hickox et al. 2009). The typically more passive galaxies expected to host radio AGNs are unlikely to be detected in the MIPS 70 μm observations used to draw our sample. Therefore, we expect that this category of AGNs will not be important for the sample selected here.

In the GOODS-N field, there are deep Very Large Array (VLA) 1.4 GHz observations reaching 3.9 μJy beam^{-1} rms with a beam size of $\sim$1$''$.7 (Morrison et al. 2010). These data were used to identify radio-excess AGNs by Del Moro et al. (2013) for counterparts of 24 μm sources which have S/N > 3 in the 1.4 GHz observation (S(1.4 GHz) > 12 μJy). Infrared SED fitting was used to compute FIR emission integrated over rest-frame $\sim$40–120 μm in order to apply a standard FIR–radio correlation.[31] Only one galaxy in our GOODS-N subsample is selected as a radio-excess source by Del Moro et al. (2013). This galaxy is also identified as AGN from all the other methods (X-ray AGN, IR AGN, and MEx-AGN) and therefore does not add a new AGN population.

In the EGS, VLA observations were presented by Ivison et al. (2007) along with a catalog of sources with S(1.4 GHz) >50 μJy ($\sim$5σ) and a $\sim$3$''$.8 FWHM synthesized beam. For the 41 radio sources with a match in the Inter/FIR sample, we computed $q_{70} \equiv \log(S_{70\,\mu\rm m}/S_{1.4\,\rm GHz})$ as a proxy for the FIR–radio correlation. The median of $q_{70} = 1.9$ is consistent to values previously reported in the same redshift range (1.9 ± 0.2 and 1.9 ± 0.1 from Frayer et al. 2006; Bourne et al. 2011, respectively) and, as expected, slightly lower than k-corrected q_{70} values (see Sargent et al. 2010 and the compilation in their Table 5). Adopting $q_{70} < 1.6$ to define radio-excess AGNs yields four AGN candidates.[32] Two of them are identified as MEx-AGNs (but undetected in X-rays and classified as SF on the IR diagnostics), while the other two are not identified as AGN by any method. One of the unidentified radio AGNs has optical signatures according to Yan et al. (2011), who assumed a more relaxed constraint on emission-line detection (S/N > 2 instead of S/N > 3 as in the current work).

Combining both GOODS-N and EGS fields gives a total of five radio-excess AGN candidates, three of which are also identified with alternative methods. The remaining two radio AGNs make only 0.7% of the Inter/FIR sample, and 1.9% of the AGN subsample. Therefore, their inclusion or exclusion does not alter the results presented in this paper, but we include them in the analysis whenever the plotted quantities are available. Namely, the two radio-AGNs that are otherwise unidentified will be put in the X-ray absorbed category (Section 5.2).

5. RESULTS

5.1. AGN Identification

The Inter/FIR sample is shown in the MEx diagram in Figure 3(a). Most (16/19 = 84%) of the X-ray AGNs lie in the MEx-AGN and MEx-intermediate regions, as expected. In addition, there are 78 AGNs identified from the MEx diagnostic that were missed in the X-ray classification, including 14 X-ray ambiguous sources.

In Figure 3(b), we compare IRAC color–color identified AGN with the X-ray and optical MEx classifications. The X-ray AGNs display a similar distribution as the optically selected AGN on the IRAC color–color plane. A few of the IRAC-AGN candidates which are undetected in X-rays are classified as AGNs with the optical diagnostic. Combining both the X-ray and MEx classifications selects 90% (9/10) of the galaxies within the IRAC selection box.

The X-ray, MEx, and IRAC color–color AGN selection methods are next shown on the IRAC single-color diagnostic described in Section 4.3 and displayed in Figure 3(c). Unsurprisingly, the FIR-selected galaxies mostly follow the tracks of the nearby infrared galaxies shown in Figure 2. Galaxies hosting X-ray AGNs span the whole range of IRAC colors covered by the Inter/FIR sample (from non-AGN and up to the most extreme AGN-like color). The X-ray AGNs that are indistinguishable from SF galaxies are likely systems where star formation dominates at infrared wavelengths even in the presence of nuclear activity (e.g., Rujopakarn et al. 2011). The IRAC single-color versus redshift diagnostic selects five AGN candidates that were not selected by the IRAC color–color diagram (panel b), including three that also lack X-ray detections. In the remainder of this paper, IRAC-selected AGNs (or simply IR-AGNs) refers to the AGNs identified from either the color–color or the single-color versus redshift method.

---

[30] The AGN templates were constructed by gathering photometry from the NASA Extragalactic Database and interpolating with templates (R. Chary 2008, private communication).

[31] This was shown by the authors to be more sensitive than using MIPS 24 μm as a monochromatic proxy of the FIR with the selection criterion of Donley et al. (2005): $q_{24} \equiv \log(S_{24\,\mu\rm m}/S_{1.4\,\rm GHz}) < 0$.

[32] This cut corresponds to a >3 σ excess according to the work of Bourne et al. (2011), and to a 1.5 σ excess according to the work of Frayer et al. (2006). The significance of the excess may thus depend on the number of galaxies and the sample selection.

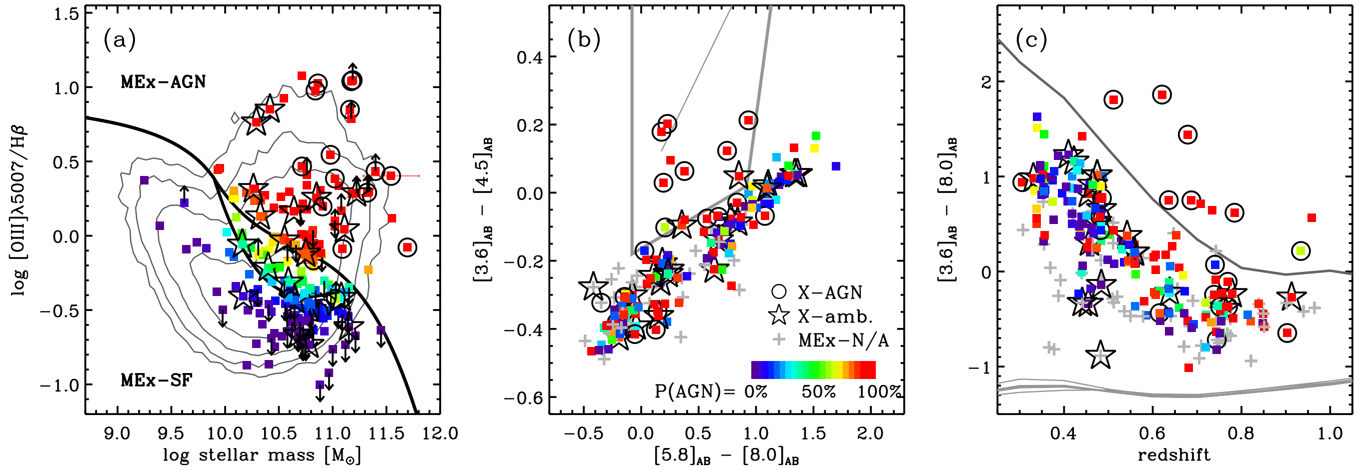

Figure 3. AGN diagnostic diagrams introduced in Figure 2: (a) the MEx-AGN diagnostic diagram. The empirical curves (solid lines) split the diagrams into galaxy spectral types as labeled, with a MEx-intermediate region between the MEx-AGN and MEx-SF classes. The contours show the SDSS low-z sample (evenly spaced logarithmically), and the 70 μm sample is superimposed with larger symbols keyed to the P(AGN) (color bar) and to the presence of X-ray AGN (circles) or ambiguous X-ray source (possibly X-ray starbursts, star symbols). (b) IRAC color–color diagram from Stern et al. (2005). The colored symbols are keyed to the MEx-AGN probabilities (color bar), whereas the gray plus symbols mark galaxies lacking a valid MEx classification due to low S/N [O III] λ5007 and Hβ lines. X-ray identified AGNs (X-ray ambiguous sources) are further marked with a circle (star symbol). Most IRAC AGN candidates in our sample are also recognized as such from the X-ray and/or MEx selection methods. (c) IRAC color as a function of redshift. The plotting symbols are the same as in the previous panel. The lower lines are the BC03 tracks for dust-free stellar populations whereas the top gray line is the template of IRAS 12112, used as an AGN–star formation dividing line in this diagram.

(A color version of this figure is available in the online journal.)

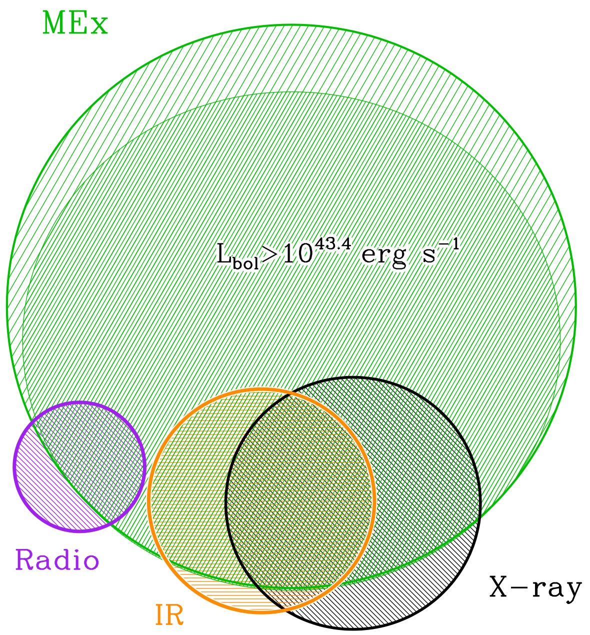

Figure 4. Venn diagram of the AGN subsamples: MEx-AGN (in green), radio-excess AGN (in purple), IR-AGN (in orange), and X-AGN (in black). The shaded areas are proportional to the number of galaxies in each category and overlap region. The MEx-AGN sample is further split into bins of AGN bolometric luminosity ($L_{\rm bol}$) as labeled. The luminosity cut at $L_{\rm bol} > 10^{43.4}$ erg s^{-1} would only remove one AGN from the IRAC AGN subsample, corresponding to 7% (1/15) of the area shown in the figure.

(A color version of this figure is available in the online journal.)

5.2. Summary of AGN Selection and AGN Properties

We illustrate the overlap and complementarity between the AGN classification methods in Figure 4. The overlap between the MEx method and the IR and X-ray methods is greater for the more luminous AGNs, as expected because they are easier to detect with any given tracer explored here. X-ray selection suffers from ambiguity between faint AGNs and starburst galaxies at low X-ray luminosities ($L_{2-10\,{\rm keV}} < 10^{42}$ erg s^{-1}, or $L_{\rm bol}$(AGN) $< 10^{43.4}$ erg s^{-1}) and the IRAC selection is mostly sensitive to intrinsically luminous and dusty AGNs ($L_{\rm bol} > 10^{43}$ erg s^{-1}; Hickox et al. 2009; Donley et al. 2012). Although optical emission lines can be subject to attenuation by dust in the host galaxy, they remain the most sensitive AGN tracer and probe to much lower accretion rates due to the detection of relatively faint emission lines in optical spectra (in this work, down to fluxes of $\sim 7 \times 10^{-18}$ erg s^{-1} cm^{-2}, corresponding to $L_{\rm bol}$(AGN) $\sim 10^{42.5}$ erg s^{-1} and accretion rates of 5×10^{-4} $M_\odot$ yr^{-1}). The greater sensitivity likely explains the additional AGN populations that are not detected with alternative methods. However, there may be cases where the NLR emission lines are extinguished by surrounding dust. It is important to combine different AGN methods to take advantage of their complementarity and achieve a more complete census. Furthermore, the combination of multi-wavelength information can distinguish between different AGN sub-populations (or AGN accretion phases).

The different AGN tracers are combined in order to divide the AGN population into three categories that are physically meaningful.

1. *X-unabsorbed AGN.* X-ray identified AGNs except for two systems that have the highest absorption ($N_{\rm H} > 10^{24}$ cm^{-2}, inferred from $\log(L_X/L_{[\rm O\,III]}) < 0.3$; see the Appendix).[33]
2. *X-absorbed AGN.* AGNs that are unidentified in X-rays—plus the two most absorbed systems excluded from the X-unabsorbed category—but which are inferred to be intrinsically luminous due to their identification with an IR or radio method or due to having $L_{[\rm O\,III]\,\lambda5007} > 10^{40.4}$ erg s^{-1}, corresponding to $L_X > 10^{42}$ erg s^{-1}. These AGNs should thus be detectable with the X-ray method in the absence of absorption.

---

[33] The remainder may contain moderately absorbed AGNs as we do not measure the absorbing column density from X-rays. The latter would be highly uncertain due to low number of counts for most objects.

Table 1
Definition of Galaxy and AGN Samples

Sample	Number	Redshift	Criteria
Low-redshift comparison galaxy sample			
Low/FIR	4034	$0.05 < z < 0.1$	S/N > 3 for Hβ, [O III] λ5007, Hα, [N II] λ6584 and [S II] $\lambda\lambda$6717, 6731 emission lines and detection in IRAS 60 μm or AKARI 90 μm
Intermediate-redshift galaxy samples			
Inter/All	9435	$0.3 < z < 1$	TKRS and DEEP2/3 spectra that cover the wavelengths of Hβ and [O III] λ5007 (from parent samples selected with R[AB] < 24.3 and 24.1, respectively)
Inter/FIR	270	$0.3 < z < 1$	Inter/All galaxies with a valid detection with MIPS 70 μm (S/N > 3)
Intermediate-redshift AGN selections			
X-AGN	19	$0.3 < z < 1$	$L_{2\text{--}10\,\mathrm{keV}} > 10^{42}$ erg s^{-1} and/or HR > −0.1
IR-AGN	15	$0.3 < z < 1$	AGN region of IRAC two-color or single-color diagram
MEx-AGN	92	$0.3 < z < 1$	MEx-AGN probabilities
Radio-AGN	5	$0.3 < z < 1$	Radio-excess (q_{70} <1.6)
Intermediate-redshift AGN samples			
X-Unabsorbed	17	$0.3 < z < 1$	X-ray identified AGNs[a]
X-Absorbed	64	$0.3 < z < 1$	X-ray unidentified AGNs[b] but intrinsically luminous [log($L_{[\mathrm{O\,III}]}$[erg s^{-1}]) > 40.4 or IR-AGN or radio-AGN][c]
Weak	18	$0.3 < z < 1$	Fail X-AGN, IR-AGN, radio-AGN selections and with weak [O III] λ5007 [log($L_{[\mathrm{O\,III}]}$ [erg s^{-1}]) < 40.4][c]

Notes.
[a] Excluding the two most extremely absorbed X-AGNs with $\log(L_X/L_{[\mathrm{O\,III}]}) < 0.3$.
[b] Including the two systems with X-AGN identification but with $\log(L_X/L_{[\mathrm{O\,III}]}) < 0.3$.
[c] Using the same conversion factors as in Section 5.2, $\log(L_{[\mathrm{O\,III}]}) = 40.4$ corresponds to $\log(L_{2\text{--}10\,\mathrm{keV}}) = 42$ and to $\log(L_{\mathrm{bol}}) = 43.4$ with luminosities in units of erg s^{-1}.

3. *Weak AGN.* AGNs that are not identified with X-rays or IRAC colors and that have a faint [O III] λ5007 luminosity ($L_{[\mathrm{O\,III}]} < 10^{40.4}$ erg s^{-1}), implying that they would not be recognized as AGNs with the X-ray definition even if they were X-ray detected.

These AGN subsamples are mutually exclusive, and the subsample sizes and definitions are summarized in Table 1. They share interesting similarities and differences in their host galaxy and accretion rate properties, and may correspond to different phases in a typical SMBH growth cycle (Section 6.3).

In what follows, we compute the distributions of AGN and SF galaxy subsamples by adding the probabilities of each galaxy falling in the category of interest. The number of galaxies per bin is the sum of $(1 - P(\mathrm{AGN}))$ for the SF subsample and the sum of $P(\mathrm{AGN})$ for the AGN subsamples. When calculating numbers, $P(\mathrm{AGN})$ is converted as a number from 0 to 1 rather than a percentage. Similarly, the probability-weighted means are obtained as follows:

$$\langle X \rangle = \frac{\sum_{i=1}^{N} X_i \times P(\mathrm{AGN})_i}{\sum_{i=1}^{N} P(\mathrm{AGN})_i}, \tag{3}$$

where X is the quantity of interest ($M_\star$, $L_{[\mathrm{O\,III}]}$, or $L_{[\mathrm{O\,III}]}/L_{\mathrm{IR}}$), and the sums are over all the N galaxies in a given subsample. $P(\mathrm{AGN})$ is replaced with $1 - P(\mathrm{AGN})$ for the SF sample. This methodology takes full advantage of the probabilistic approach of the MEx diagram.

As can be seen in Figure 5, X-unabsorbed AGNs are only found in the most massive hosts ($\sim 10^{10.6}$–$10^{12}\ M_\odot$), whereas X-absorbed and weak AGNs span a broader range of stellar masses ($\sim 10^{10}$–$10^{12}\ M_\odot$) and have a similar average stellar mass as the non-AGN galaxies in the Inter/FIR sample ($\sim 10^{10.6}\ M_\odot$), which is $\sim$0.5 dex lower than the average stellar mass of the X-unabsorbed sample. The apparent lack of X-unabsorbed AGNs in lower mass hosts may be due to a combination of AGN evolutionary phase and selection bias (discussed in Section 6.3).

Absorbed and X-unabsorbed AGNs have similar AGN luminosities on average ($L_{\mathrm{bol}}(\mathrm{AGN}) \sim 10^{44}$ erg s^{-1}; inferred from [O III]; Figure 5) and are systematically higher (by 1 dex on average) than the weak AGNs and the SF galaxies. The physical meaning of $L_{\mathrm{bol}}(\mathrm{AGN})$ does not apply to the SF subsample (unless the galaxies contain unidentified AGNs). However, the similarity of the [O III] luminosities between weak AGNs and SF galaxies (similar means, and relatively similar distributions) implies that we are able to distinguish between these two populations based on an additional factor and that the [O III] luminosity alone is not sufficient to discriminate between AGNs and SF galaxies. This may be because [O III] may contain a contribution from low-metallicity gas ionized by star formation. This contribution is expected to be negligible in metal-rich galaxies (Kauffmann et al. 2003), but we test this possible contamination to [O III] by examining the [O III]-to-IR luminosity ratios. If the [O III] emission traced the SFR instead of the AGN luminosity, and assuming that L_{IR} traces the SFR, we would expect similar ratios between SF galaxies and the false AGN candidates. In the case of genuine BH growth with small or no stellar contribution to [O III], the [O III]-to-IR ratios can be converted as black hole accretion rate (BHAR) to SFR ratios. Absorbed and X-unabsorbed AGNs have similar BHAR-to-SFR ratios, and are systematically higher (by 0.5–0.6 dex) than the weak and SF subsamples indicating an [O III] excess emission (Figure 5). The later two subsamples exhibit similar [O III]-to-IR distributions to one another, suggesting that the weak AGNs are not only weak relative to the absorbed and X-unabsorbed subsamples, but also relative to the SFR of their hosts. Some of the weak AGNs may represent a distinct AGN regime with possibly radiatively inefficient accretion (Ptak et al. 1998; Ho 2008; Trump et al. 2011) rather than a simple extension of the same accretion process down to lower luminosity (but also see Maoz 2007).

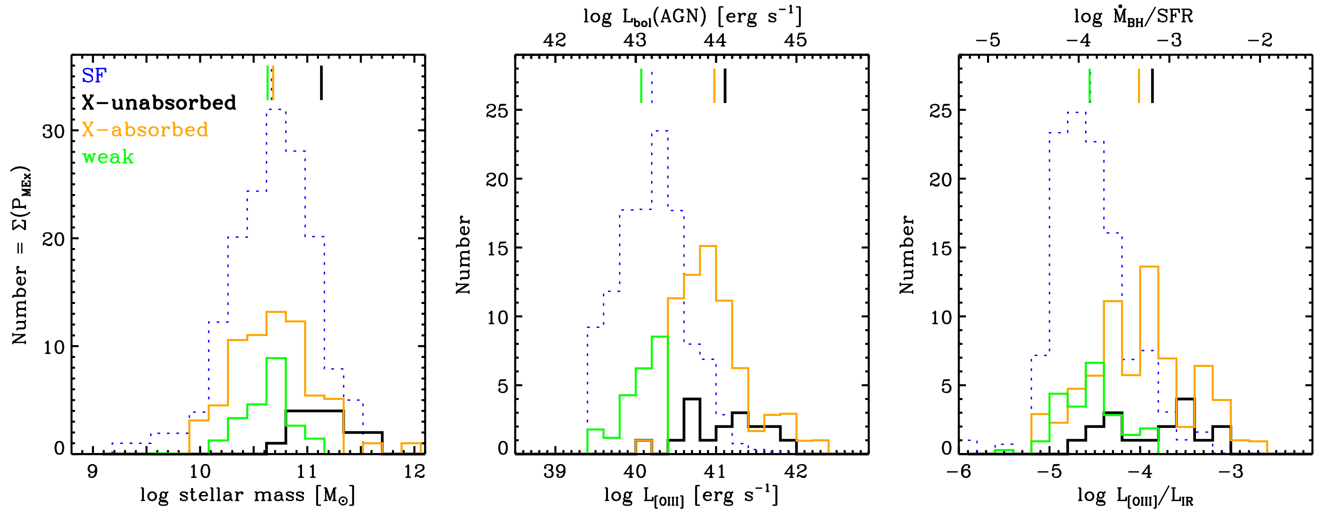

Figure 5. Distribution of host galaxy stellar masses (left), [O iii] luminosities (center; corresponding AGN bolometric luminosities on the top axis), and [O iii]-to-IR luminosity ratios (right; corresponding BHAR-to-SFR ratios on the top axis). Those properties are shown for star-forming galaxies (blue dotted line) and the three AGN subsamples: X-unabsorbed (black), X-absorbed (orange), and intrinsically weak (green). The physical meaning of $L_{\rm bol}$(AGN) and BHAR does not apply to the SF subsample (unless some of those galaxies contain unidentified AGNs). The *number* of galaxies is computed with $\sum(1 - P({\rm AGN}))$ for the SF subsample and with $\sum P({\rm AGN})$ for the AGN subsamples (as a reminder, $P({\rm AGN}) = P_{\rm MEx}({\rm AGN})$ for MEx-only AGNs and $P({\rm AGN}) = 1$ for X-AGNs and IR-AGNs). The probability-weighted means (Equation 3) are indicated with vertical lines.

(A color version of this figure is available in the online journal.)

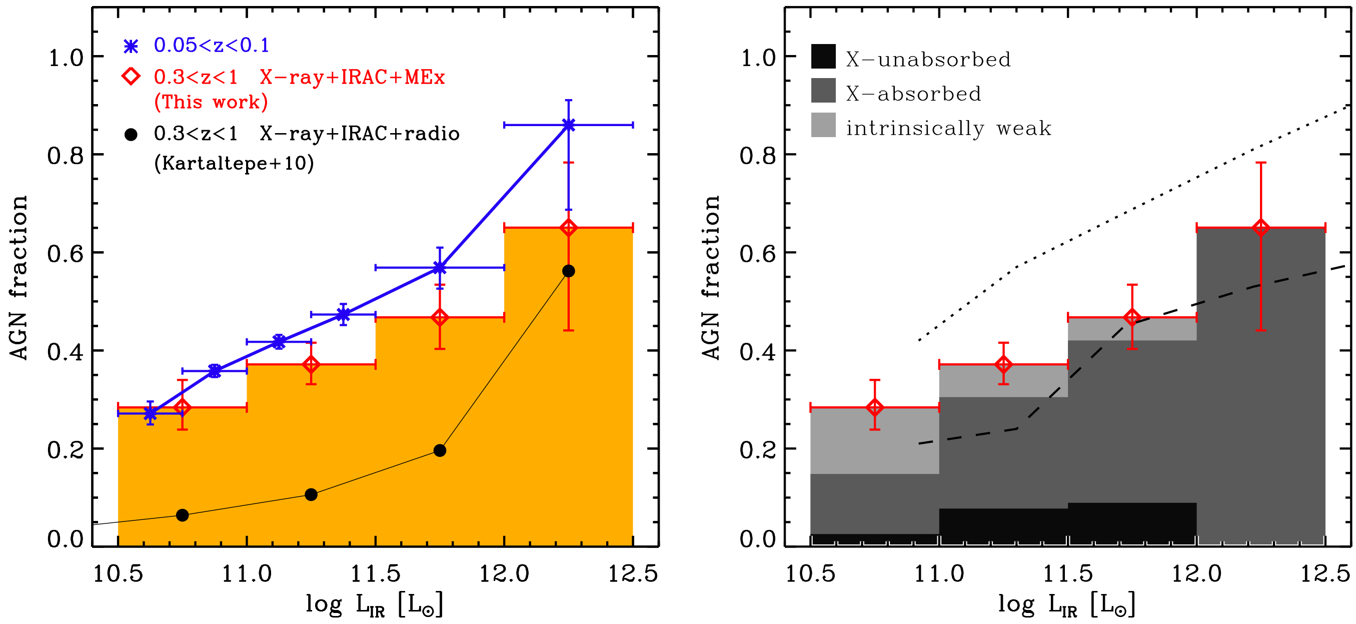

Figure 6. Left: AGN fraction as a function of $L_{\rm IR}$ in intermediate-redshift FIR-selected galaxies (filled histogram). The AGN fraction rises with increasing $L_{\rm IR}$ in agreement with the trend observed for low-redshift ($0.05 < z < 0.1$) FIR-selected SDSS galaxies from Hwang et al. (2010a, shown in blue). For comparison, we also show values obtained for the 70 μm selected sample from Kartaltepe et al. (2010a), spanning similar luminosity and redshift ranges (filled black symbols). Right: similar to the left-hand panel except that the AGN content is broken down into X-ray unabsorbed, X-ray absorbed, and intrinsically weak systems, as labeled. Interestingly, the overall trend of the AGN fraction against $L_{\rm IR}$ resembles that of the galaxy merger fraction (dashed line) and the combined irregular and merger morphology fraction (dotted line) observed by Kartaltepe et al. (2012) at $z \sim 1$ (discussed in Section 6.4). The horizontal error bars show the bin width and vertical error bars show the 68.3% confidence intervals for fractions, determined with Bayesian binomial statistics following the formalism of Cameron (2011).

(A color version of this figure is available in the online journal.)

5.3. *AGN Fraction in Intermediate-redshift Infrared Galaxies*

In order to obtain the global AGN fraction, we combine all of the AGN identification methods, namely, the MEx diagnostic diagram, the X-ray classification, and the IRAC single-color and two-color diagrams. Adopting the procedure from Section 4.2 and Equation (2), the global AGN fraction in $0.3 < z < 1$ FIR-selected galaxies is 37% ± 3% (99/270).

The AGN fraction increases steadily with $L_{\rm IR}$ and both the increase and the magnitude of the AGN fraction are consistent with the values obtained for the low/FIR comparison sample (Figure 6). The similarity between the AGN fractions of the Low/FIR and Inter/FIR samples is consistent with no or very mild evolution in the triggering of AGN as a function of IR luminosity between $z \sim 1$ and $z \sim 0$.

In contrast, the AGN fraction found for the Inter/FIR sample is significantly higher than that of similarly selected galaxies in the COSMOS field (Kartaltepe et al. 2010a). Those authors combined X-ray, IRAC power law, and radio AGN identification methods (also see Symeonidis et al. 2010) but lacked a robust

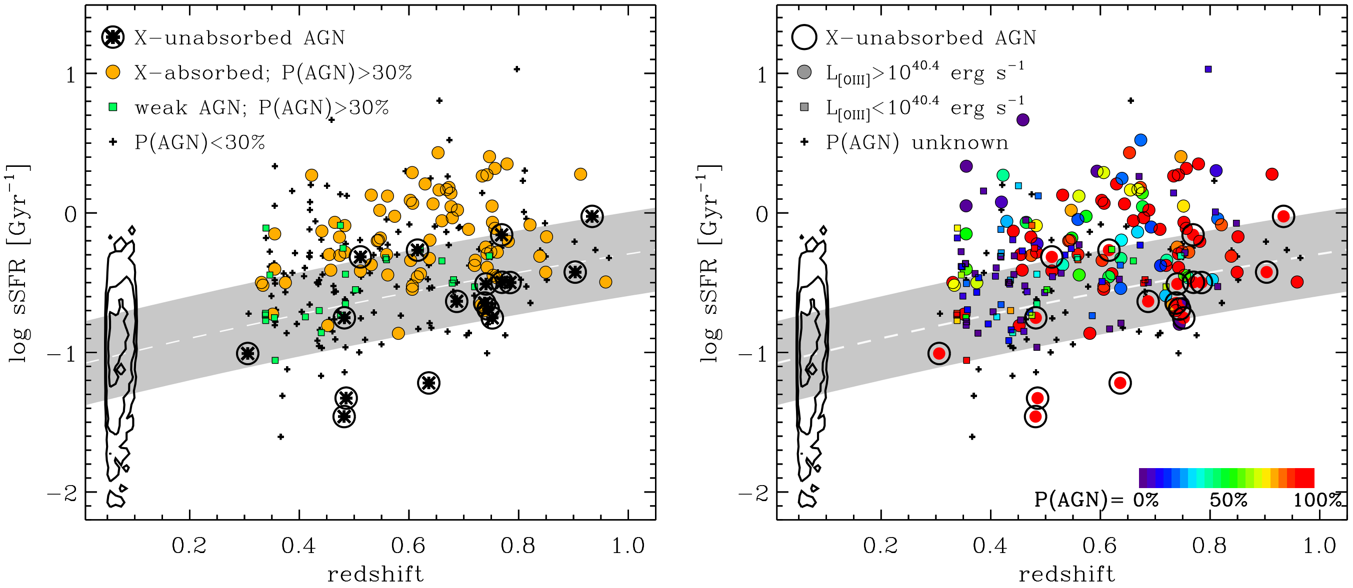

Figure 7. Left: sSFR as a function of redshift. The inter/FIR galaxy sample spans the *sSFR sequence*, shown with a gray shaded area, and beyond. X-ray unabsorbed AGNs (black asterisks) mostly lie on or below the sSFR sequence, whereas X-ray absorbed AGNs (orange circles) and intrinsically weak AGNs (green squares) tend to have higher sSFRs. The latter are shown only for objects with an AGN probability percentage >30% but the right-hand panel conveys the information on the individual P(AGN) percentages. Right: the same as left panel, except that the symbols are color-coded according to P(AGN) when available (otherwise shown with black plus symbols). The shape of symbols indicates the [O III] luminosity (filled circles if $>10^{40.4}$ erg s^{-1}; filled squares otherwise). X-ray unabsorbed AGNs are furthermore marked with large open circles. The contours indicate the distribution of the Low/FIR sample on the sSFR–z plane.

(A color version of this figure is available in the online journal.)

optical emission line diagnostic.[34] Our higher AGN fractions are mostly a result of a more complete AGN selection due to the inclusion of X-ray faint and absorbed AGNs from the MEx diagram. The latter account for most of the difference between the samples (right panel of Figure 6).

There are more X-ray absorbed AGNs than X-ray unabsorbed AGNs at all IR luminosities but the distributions of the infrared luminosities of these two AGN categories are similar. The intrinsically weaker AGNs tend to reside in less infrared-luminous hosts. The dearth of intrinsically weak AGNs in the most luminous galaxies may be due to increased dilution by star formation and not necessarily caused by a difference in the triggering mechanisms. If we missed AGN due to star formation dilution, our AGN census would be more incomplete at the IR-luminous end. However, we already observe a larger AGN fraction in more IR-luminous systems, which is opposite to the effects of dilution or dust obscuration. Thus, the observed increase in AGN fraction with $L_{\rm IR}$ is robust despite this potential bias.

5.4. AGN on the SFR–$M_\star$ Sequence

The high incidence of AGN in infrared-luminous hosts may hint at a link between BH growth and SFR. The SFR is known to evolve with redshift and to correlate strongly with stellar mass at a given redshift. The correlation between the SFR and stellar mass has been reported in several studies (e.g., Brinchmann et al. 2004; Noeske et al. 2007; Elbaz et al. 2007). Assuming a linear relation between SFR and stellar mass at a given redshift,[35] the evolution of the normalization has been parameterized by Elbaz et al. (2011) as

$$\mathrm{sSFR}_{\mathrm{sequence}}(z)\ [\mathrm{Gyr}^{-1}] = 26 \times t_{\mathrm{cosmic}}^{-2.2}, \qquad (4)$$

where $t_{\rm cosmic}$ is the cosmic time in Gyr at the redshift z of interest. Here, we study the sSFR of the AGN hosts relative to the remainder of the inter/FIR sample. The X-ray unabsorbed AGNs tend to reside in galaxies on or slightly below the sSFR sequence, in agreement with results from Mullaney et al. 2012), while the X-ray absorbed and/or X-ray weak AGNs are hosted by galaxies with higher sSFRs (Figure 7).

The overall AGN fraction appears to be independent of both the sSFR and Δlog(sSFR), the relative offset from the redshift-dependent sSFR sequence:

$$\Delta \log(\mathrm{sSFR}) \equiv \log(\mathrm{sSFR}) - \log(\mathrm{sSFR}_{\mathrm{sequence}}(z)) \qquad (5)$$

(Figure 8). In contrast to the near constancy of the AGN fraction with respect to the sSFR, we find a strongly increasing fraction of X-ray absorbed AGNs among the moderately luminous AGN population as sSFR (or Δlog(sSFR)) increases. Combined, these results suggest that the AGN obscuration depends strongly on the sSFRs of the host galaxies, but the total incidence of AGNs (probed by the AGN fraction) does not.

5.5. X-Ray Absorbed AGN

As shown in Section 5.3 and summarized in Table 1, X-ray absorbed AGNs are more common in actively SF (FIR-selected) galaxies (24%) than X-ray unabsorbed AGNs (7%). In what follows, we define the absorbed AGN fraction as the number of X-absorbed AGNs over the combined number of X-absorbed and X-unabsorbed AGNs, i.e., without taking into account the intrinsically weak systems. The behavior of BH growth and AGN absorption is investigated as a function of host galaxies' properties in Figure 9. The occurrence of AGN increases with infrared luminosity, tracing SFR, and is fairly flat

---

[34] Symeonidis et al. (2010) used a simple [O III] $\lambda5007/\mathrm{H}\beta > 3$ threshold, which only selects AGNs with the most extreme line ratios. This selection criterion would yield only 10 out of 92 (11%) MEx-AGNs.

[35] The index α of the relation SFR $\propto M_\star^\alpha$ is consistent with unity within the uncertainties and within the spread of values published in the literature but the exact value and whether it changes with redshift remains under debate.

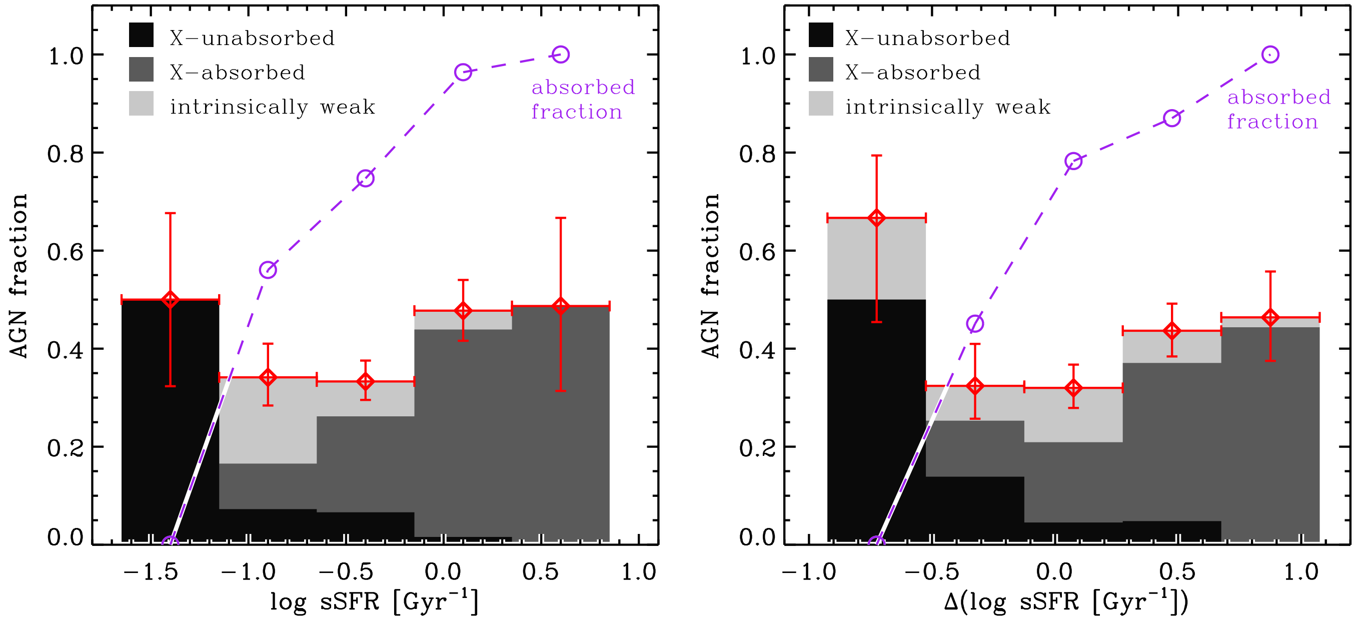

Figure 8. Left: fraction of galaxies hosting active nuclei as a function of their sSFR (red diamonds). Right: fraction of galaxies hosting active nuclei as a function of their distance from the sSFR sequence (red diamonds). In both panels, the AGN categories are distinguished with the shades of gray as labeled. The X-ray absorbed fraction among the moderately luminous AGN population (e.g., excluding the weak AGN category) is shown with the open circles and dashed purple line. The horizontal error bars show the bin width and vertical error bars show the 68.3% confidence intervals for fractions, determined with Bayesian binomial statistics following the formalism of Cameron (2011).

(A color version of this figure is available in the online journal.)

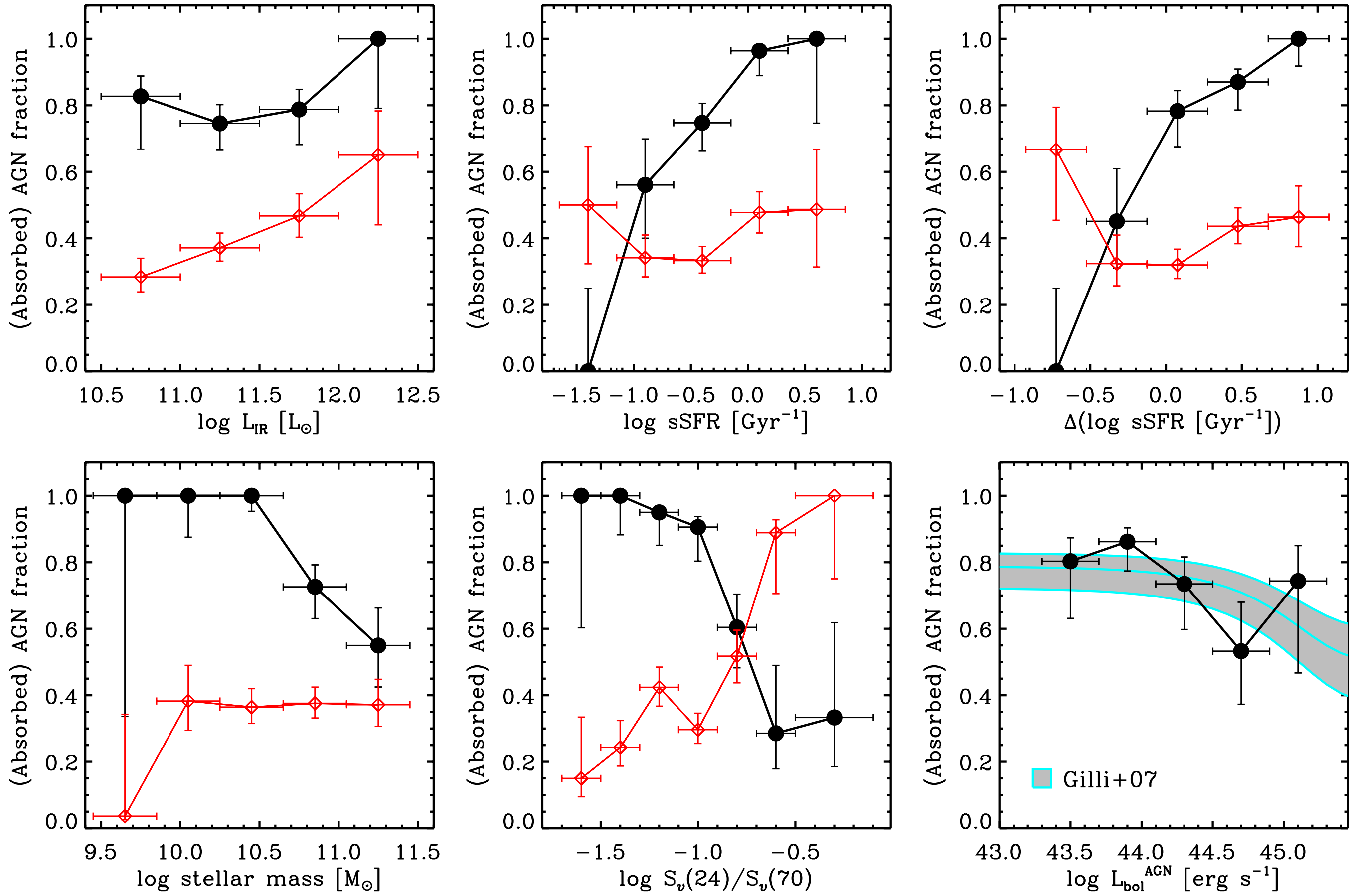

Figure 9. AGN fraction (red diamonds) and fraction of the AGNs that are X-ray absorbed (filled black circles) as a function of the following parameters: infrared luminosity, specific SFR, distance from the sSFR sequence (ΔsSFR), stellar mass, mid- to far-infrared color, and AGN bolometric luminosity. In the last panel, the X-ray obscured fraction from Gilli et al. (2007) is shown with the shaded area, where we applied the same bolometric correction factor to the X-ray luminosity as in the rest of this work (1.4 dex). The horizontal error bars show the bin width and vertical error bars show the 68.3% confidence intervals for fractions, determined with Bayesian binomial statistics following the formalism of Cameron (2011).

(A color version of this figure is available in the online journal.)

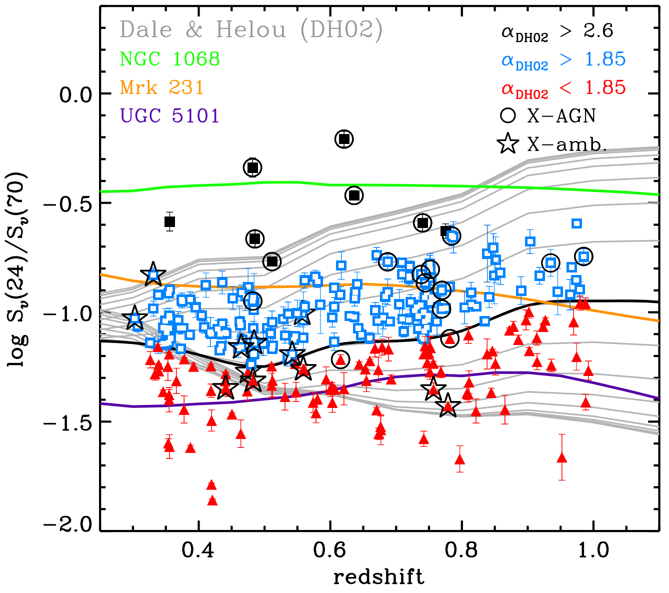

Figure 10. Observed 24-to-70 μm flux density ratio as a function of redshift for galaxies in GOODS-N and EGS. The observed values are compared directly to redshifted model templates from Dale & Helou (2002), applicable to star-forming galaxies (gray lines). The black line shows the DH02 template chosen to split our sample between high S_{24}/S_{70} (blue squares) and low S_{24}/S_{70} ratios (red triangles), with the most extreme S_{24}/S_{70} highlighted with filled black squares. X-ray AGNs and X-ray ambiguous sources are, respectively, marked with open circles and star symbols. For visual comparison, we include redshifted tracks for three nearby AGNs: NGC 1068 (Seyfert 2, in green), Mrk 231 (Seyfert 1, in orange), and UGC 5101 (obscured or buried AGN, in purple).

(A color version of this figure is available in the online journal.)

with stellar mass (with a possible drop below 10^{10} $M_\odot$ but the uncertainty in the lowest mass bin is too large to conclude, due to incompleteness at such low masses). Interestingly, the AGN fraction against the sSFR is consistent with a constant value around ∼35% on and outside the sSFR sequence. Lastly, the AGN fraction increases with warmer 24-to-70 μm colors as expected from an AGN contribution to dust heating (Section 5.6).

The behavior of the absorbed AGN fraction differs from that of the occurrence of AGNs in galaxies. The fraction of AGNs that are absorbed is fairly constant with IR luminosity with perhaps a mild increase at the highest L_{IR}, while it decreases with increasing stellar mass, and increases sharply with increasing sSFR. These trends suggest that AGN X-ray absorption may not be as sensitive to the total gas mass (somewhat traced by L_{IR}) as to the gas fraction and/or gas density, traced by sSFR. The absorbed fraction decreases with warmer 24-to-70 μm colors, suggesting a smaller relative contribution of star formation in less absorbed AGNs. Lastly, the absorbed fraction decreases with increasing bolometric luminosity of the AGN, in agreement with results reported previously (e.g., Ueda et al. 2003; La Franca et al. 2005; Trump et al. 2009). Gilli et al. (2007) proposed an analytical description of the absorbed fraction adjusted to represent the data points of Ueda et al. (2003) and La Franca et al. (2005) with their model m2, shown in the bottom right panel of Figure 9.

5.6. *Effect of AGN on Mid- to Far-infrared Color*

The observed 24-to-70 μm flux ratios of the Inter/FIR galaxy sample span a broad range of values (Figure 10), extending beyond the range of the IR SED templates from Dale & Helou (2002, hereafter DH02), especially at lower redshift.[36] We use the DH02 template that splits the sample in comparable numbers on either side as a redshift-dependent dividing line between galaxies with high and low S_{24}/S_{70} galaxies. The chosen template has a parameter $\alpha = 1.85$, where α is the index of the power law relating the mass of dust heated to the intensity of the interstellar radiation field responsible for the heating; see Equation (1) of DH02. According to the method described by Marcillac et al. (2006), this SED corresponds to a total infrared luminosity of 10^{11} $L_\odot$. X-ray identified AGNs tend to reside above the line and reach the largest values of S_{24}/S_{70}.

With Figure 11, we study the mid- to far-infrared color of the AGN hosts (including X-ray, IR, and MEx-AGNs) with respect to the rest of the SF galaxies in our sample. Galaxies with a low S_{24}/S_{70} (red triangles) predominantly occupy the SF and intermediate regions of the MEx diagram (panel a), and the SF region of the IRAC two-color diagram (panel b). Galaxies with a high S_{24}/S_{70} (blue squares) are distributed across the full range of parameter space with the most extreme cases (filled black squares) almost exclusively classified as AGN on the MEx diagram, and in or near the AGN region on the IRAC two-color diagram. Galaxy mid- to far-infrared colors are more evenly distributed on the IRAC single-color diagram (panel c) but there is an excess of the most extreme infrared colors (filled black squares) in the AGN region. Overall, galaxies with the highest S_{24}/S_{70} values are much more likely to be identified as AGNs with any (or all) of the AGN tracers, especially X-rays and optical lines. This result indicates that the active nuclei within these galaxies significantly contribute to the heating the dust whose emission is measured by the 24 and 70 μm passbands at these redshifts.

The AGN-heated contribution to dust emission is expected to peak at shorter wavelengths (∼10–20 μm) compared to dust heated by star formation processes, and hence produce an enhanced mid- to far-IR ratio. The average AGN SED template of Elvis et al. (1994) suggests this feature (see also Mullaney et al. 2011, for the intrinsic AGN IR SED of more moderate luminosity AGN). Veilleux et al. (2002) found that the spectra of nearby ULIRGs with warmer IRAS 25-to-60 μm color ($S_{25}/S_{60} > 0.2$) are quasar-like, whereas the spectral features of cooler ULIRGs are similar to LINER or purely SF galaxies. Similarly, we observe that the galaxies with the highest S_{24}/S_{70} values were selected as X-ray AGN (Figure 10), MEx-AGN (Figure 11(a)) and mostly also as IRAC AGN (Figures 11(b) and (c)). The expectations appear to hold well for these few extreme systems, but whether there is also a trend for the more normal, less extreme AGNs is less clear.

Figure 12 presents another diagnostic by combining the [O III] λ5007/Hβ and S_{24}/S_{70} ratios. There are 202 galaxies in our sample with all required measurements, including galaxies with an upper limit for either [O III] λ5007 or Hβ (but not both). The bulk of the sample tends to occupy the bottom left part of the plot with several outliers toward the upper right, which are the more extreme and easily identified AGNs (according to at least one of the X-ray and the MEx classification schemes).

We define an empirical curve to divide the region dominated by X-ray AGNs from the rest of the sample:

$$\log([\mathrm{O\,III}]/\mathrm{H}\beta) = \frac{0.6}{\log(S_{24}/S_{70}) + 0.28} + 1.2. \tag{6}$$

---

[36] The DH02 models were constructed using IRAS sources, and so are deficient in galaxies whose FIR is dominated by cold dust such as those selected in longer wavebands with, e.g., *Herschel* (Smith et al. 2012).

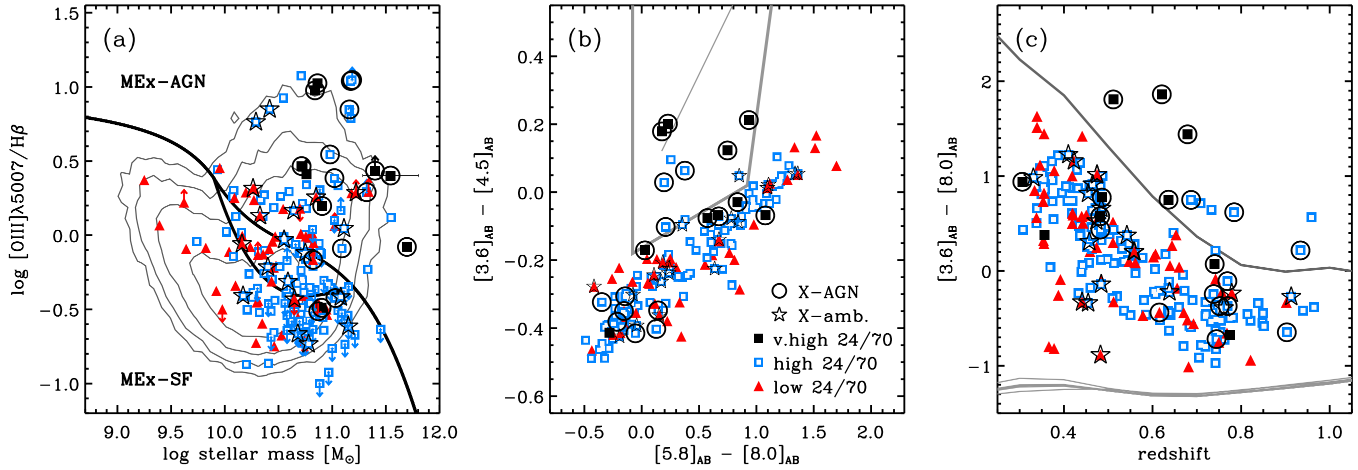

Figure 11. AGN diagnostic diagrams introduced in Figure 2. The symbols are keyed to the mid- to far-infrared color S_{24}/S_{70} (red triangles for low values; open blue squares for high values; filled black squares for very high values) and to the X-ray classification (open circles for X-AGN and open star symbols for X-ambiguous). (a) The MEx-AGN diagnostic diagram. The empirical curves (solid lines) split the diagrams into galaxy spectral types as labeled, with a MEx-intermediate region between the MEx-AGN and MEx-SF classes. The contours show the SDSS low-z sample (evenly spaced logarithmically). Objects with low values of S_{24}/S_{70} tend to be centrally distributed on the MEx diagram, while the location of the high-S_{24}/S_{70} galaxies extends to both extremes of the [O III]/Hβ range. Galaxies with very high S_{24}/S_{70} are exclusively on the AGN tail of the distribution toward high values of [O III]/Hβ. (b) IRAC color–color diagram with the AGN region (thick solid line) defined by Stern et al. (2005), and the power locus (thin solid line) by Donley et al. (2007). Galaxies with the highest S_{24}/S_{70} are located within or nearby the boundaries of the AGN region, as expected if there were a 24 μm excess caused by AGN-heated dust emission. (c) IRAC color as a function of redshift. The AGN candidates lie above the dark gray dividing line and span a broad range of S_{24}/S_{70} values although 72% (13/18) have high or very high ratios (open and filled squares). The light gray tracks at the bottom define the lower envelope expected from BC03 stellar population templates with no dust emission.

(A color version of this figure is available in the online journal.)

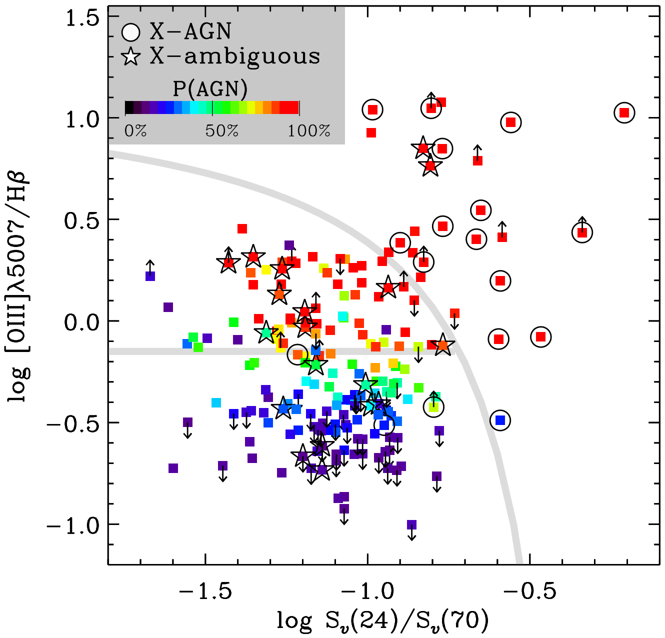

Figure 12. Combined optical/IR diagram showing the [O III] λ5007/Hβ emission-line flux ratio as a function of a mid- to far-IR color (24-to-70 μm). The 70 μm galaxy sample was classified based on the MEx diagram (color keyed to P(AGN) as shown on color bar) as well as from their X-ray properties (star symbols for X-ray starbursts/ambiguous systems, and black circles for X-ray AGNs). The lines represent an empirical division between the most extreme AGNs (top right), the more common AGNs (middle), and star-forming galaxies (bottom left).

(A color version of this figure is available in the online journal.)

A dividing line at fixed [O III]/Hβ ratio (log([O III]/Hβ) = −0.15) separates the optically selected AGNs (green to red colored symbols) from the SF galaxies (purple to blue colored symbols). Given the fact that the galaxies between the lines are not detected in hard X-rays and given their range of [O III]/Hβ values, they may be composite SF/AGN galaxies and possibly LINERs (though we expect very few LINERs given the FIR selection; see, e.g., Yuan et al. 2010). Interestingly, the X-ray undetected AGN candidates and SF galaxies appear to have a very similar distribution in their 24-to-70 μm colors. These systems may have a weak AGN whose contribution to the dust emission is small, or a more luminous AGN concurrent with an elevated SFR and thus also resulting in a small *relative* contribution. Alternatively, the IR SED shape might have a more complicated dependence on AGN heating owing to the geometry of the system. More generally, this result implies that factors other than the presence of AGN should be taken into account in order to explain the spread in S_{24}/S_{70} values.

This analysis is analogous to that presented by Kewley et al. (2001), where the authors derived a mixing line going from low values of IRAS 25/60 μm flux ratio and [O III]/Hβ ratio toward higher values as the AGN fraction increases. Furthermore, they found AGN fractions of 73% and 77% in galaxies with $\log(S_{25}/S_{60}) > -0.6$ and −0.5, respectively. Although probing somewhat different rest-frame wavelengths, our results are consistent with the same general picture, as all galaxies with $\log(S_{24}/S_{70}) > -0.6$ satisfy our AGN selection criteria. The results of increasing incidence of AGN in systems with warmer mid- to far-infrared colors from Kewley et al. (2001) and Veilleux et al. (2002) were derived for nearby galaxies. Figure 12 is the higher-redshift analog.

The overall trend between the presence of AGN and the mid- to far-IR color S_{24}/S_{70} is shown in Figure 13, where the AGN fractions are calculated using the same methodology as in Section 5.3. We find an increasing AGN fraction with warmer S_{24}/S_{70} values. While the warm color side appears to be driven by X-ray-detected AGNs, removing these objects from the sample reduces the linear Pearson coefficient only from 0.94 to 0.88. Overall, we thus recover the expected trend from dust heating by AGN in the sample of FIR-selected galaxies used in this work.

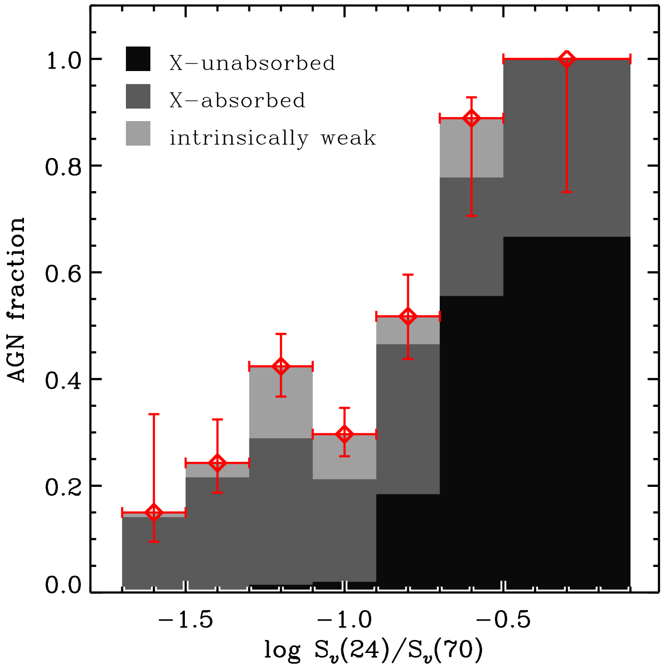

Figure 13. AGN fraction as a function of mid- to far-IR color (24-to-70 μm). The FIDEL 70 μm galaxy sample was classified as AGN based on all of the AGN diagnostics used in this paper: X-rays, MEx diagram, and IRAC colors. The split into AGN sub-categories is described in Section 5.3 and is identical to the right panel of Figure 6. The horizontal error bars show the bin width and vertical error bars show the 68.3% confidence intervals for fractions, determined with Bayesian binomial statistics following the formalism of Cameron (2011).

(A color version of this figure is available in the online journal.)

6. DISCUSSION

6.1. *Caveats*

There are three main caveats in this analysis although none of them is expected to significantly alter our results. The first is that total infrared luminosities, which we interpret as measures of SFR, contain mixed contributions from dust heated by both stars and AGNs. While longer wavelengths (70 μm) are less subject to AGN contamination than, say, 24 μm, they can still have non-zero contribution from AGN-heated dust emission. Recent *Herschel* studies have shown that the FIR colors of galaxies with an AGN do not differ from those of purely SF galaxies (Hatziminaoglou et al. 2010; Elbaz et al. 2010), indicating that on average AGN contamination does not dominate at λ(observed) $\geqslant$ 70 μm. We mitigate against this effect by not using the shorter wavelength data ($\lambda \leqslant 24\,\mu$m) when calculating $L_{\rm IR}$ for the FIR-selected sample (Section 2.5).

The second caveat concerns the overall completeness of the AGN selection methods used in this work. As mentioned in Section 5.3, some objects have an unknown classification because of the low S/N of their emission lines. As a consequence, the AGN fraction that we derive for the overall FIR-selected sample (i.e., with and without emission-line detections) may be underestimated as we consider these unclassified galaxies to be purely SF unless they fulfill the X-ray or IR AGN selection criteria. Taking into account that some of the unknown class are AGNs would strengthen our conclusion that AGNs are ubiquitous among FIR-selected galaxies given that we already find a large AGN fraction. We computed a maximum AGN fraction assuming that all of the unknown class galaxies host an AGN: it would rise from 37% to 62%, but this scenario is unlikely given that the unknown galaxies do not fulfill the emission-line criteria and that emission-line galaxies were shown to have a higher incidence of AGN than their non-emission-line counterparts (e.g., Yan et al. 2006). We test this trend with our own sample by comparing the X-ray and IRAC AGN fractions for the global FIR sample and the emission-line FIR sample. These methods suggest a 2× higher AGN fraction in emission-line galaxies. There are 12^{+4}_{-2}% (18/145) X-AGN and IRAC-AGN in the emission-line subsample, but only 6% ± 2% (7/125) in the remaining subsample, resulting in a global fraction of 9% (25/270) when considering all FIR-selected galaxies regardless of the detection of [O III] and Hβ emission lines. Among objects with AGN classifications, it is also possible that the MEx diagnostic diagram misses AGNs preferentially in low-mass galaxies, especially if there is also ongoing star formation diluting AGN emission signatures. Such AGNs are fairly rare in the nearby universe but would not be accounted for if they were more common at higher redshift.

The third caveat concerns the use of [O III] λ5007 as an indicator of AGN bolometric luminosity. On the one hand, [O III] emission could include a contribution from star formation yielding an overestimate of the total AGN power. This is a more serious concern for low-metallicity galaxies. Kauffmann et al. (2003) found that in high-metallicity galaxies, the [O III] λ5007 line is the least contaminated of the strong emission lines measured in optical spectra, with a flux fraction of 7% from star formation and the remaining 93% from AGN-induced emission. The stellar mass–metallicity ($M_\star$–Z) relation (Tremonti et al. 2004) furthermore implies that metal-poor galaxies have small stellar masses. Given that all the FIR-selected galaxies are fairly massive, they likely have a fairly elevated metallicity and their [O III] lines are likely dominated by AGN emission. However, the mass–metallicity relation has been shown to evolve with redshift (Savaglio et al. 2005) and/or SFRs of the galaxies (Mannucci et al. 2010) in the sense that the galaxies in the current sample could have a slightly lower metallicity than galaxies of like stellar masses in the nearby universe. We thus compared $L_{\rm [O\,III]}$ to $L_{\rm IR}$, tracing the SFR, in order to check whether the MEx-AGNs present [O III] excess due to their elevated SFRs rather than true AGN excitation. Both X-ray absorbed and unabsorbed AGNs show the same [O III]-to-IR excess with respect to the subsamples of weak AGNs and SF galaxies (Figure 5).

On the other hand, [O III] λ5007 emission may be affected by dust obscuration. Even though we use [O III] as a more isotropic tracer than 2–10 keV, it is not in fact perfectly isotropic (e.g., Diamond-Stanic et al. 2009). Dust obscuration would have the opposite effect, and would lead to an underestimate of the intrinsic AGN luminosity when not applying a correction for extinction. We conservatively choose not to correct for dust obscuration, which means that the X-ray absorption may be underestimated and similarly, the number of absorbed AGNs may be a lower limit. Given that we already find a high incidence of absorbed AGNs among FIR-selected galaxies, our result would only be strengthened if we indeed underestimated the number of absorbed AGNs.

6.2. *Link between AGN Obscuration and Host Galaxies*

A high absorbed fraction among AGNs at high redshift may be expected because in addition to small-scale (torus) absorption, there were important gas reservoirs in galaxies at $z > 1$ (Daddi et al. 2010; Tacconi et al. 2010) that can potentially contribute to absorbing X-rays. Models of gas-rich galaxies predict high column densities (reaching the Compton-thick regime with $N_{\rm H} > 10^{24}$ cm^{-2}) along several lines of sight in both isolated gas-rich unstable disks (Bournaud et al. 2011) and in major mergers (e.g., Hopkins et al. 2006). Furthermore, analyses of the cosmic X-ray background infer an important population of X-ray absorbed AGNs at $z < 1$ (Comastri et al. 1995; Merloni 2004). Therefore, a high fraction of hidden AGNs should be expected at increasing redshift.

Is the absorption occurring on small scales or galaxy scales or both? In the former case, one would expect that AGN absorption would not correlate with galaxy-scale properties.[37] Interestingly, we found that the fraction of the AGNs that are absorbed increases sharply with the sSFRs (Figure 9). Before discussing the physical implications, we further examine X-ray absorption in relation to the infrared luminosities of the host galaxies with an extension to fainter host galaxy samples.

We start from AGNs that have both X-ray and [O III] detections in the Inter/All sample (dubbed the X + [O III] sample), and divide this population according to their detections in the MIR only (FIDEL 24 μm) or in the FIR (FIDEL 70 μm). The 24 μm comparison sample has a much fainter ($\sim 10\times$) $L_{\rm IR}$ sensitivity limit than the 70 μm sample (Figure 1). The remainder of the X-ray+[O III] AGN sample lacks FIDEL 24 μm detections and thus probes yet lower IR luminosities. These three subsamples have significant differences in sensitivity in terms of the SFR of their hosts but we otherwise constrain this portion of the analysis to galaxies that have $\log(M_\star) > 10^{10}\ M_\odot$ and $P({\rm AGN}) > 30\%$.[38] With comparable masses and fairly secure AGNs, the 70 μm subsample will include galaxies with the highest sSFRs whereas the 24 μm and X+[O III] subsamples probe down to lower sSFRs given a range of masses and redshifts.

The distributions of the Compton-thickness parameter ($\log T \equiv \log(L_{2-10\,{\rm keV}}/L_{\rm [O\,III]})$) between the FIR (70 μm), MIR (24 μm), and X + [O III] samples are shown in Figure 14. The FIR-selected subsample tends to host more absorbed AGNs than either of the comparison samples. If the parent population of the FIR (light gray) and X + [O III] (black line without the light gray area) subsamples were the same, the probability of drawing both distributions would be 0.0012% according to a K-S test. It remains very low (0.038%) for the distributions of the FIR- and MIR-selected subsamples. The distribution of the latter is intermediate between the X + [O III] subsample and the most IR-luminous (detected at 70 μm) sample. Clearly, the majority of the most absorbed systems (with Compton thickness $\log(T) < 0.3$; see the Appendix) tend to be infrared-luminous given their high detection rate at 70 μm.

The overall trend is more frequent AGN X-ray absorption in galaxies with higher sSFRs. In order for this trend to be caused by geometry of the putative torus from AGN unified models, the small-scale obscuring torus would have to be physically and/or optically thicker in FIR-luminous galaxies with elevated sSFR. Another possibility is that (part of) the gas reservoir available to sustain the elevated SFR also acts as an important absorber for the central AGN. This situation could be increasingly common at higher redshifts as the AGN hosts show an increase in SFR (Mullaney et al. 2010; Shao et al. 2010; Mullaney et al. 2012). Our findings imply that it is not just the total SFR (or $L_{\rm IR}$) that is relevant but rather the sSFR. This points to another factor explaining the apparent connection between AGN X-ray absorption and host galaxies. We postulate that it could be in part because the sSFR can trace the gas fraction across the sSFR sequence (but no longer when reaching the more extreme sSFRs; Magdis et al. 2012), and because for the more extreme objects above the main sequence, the enhanced sSFR could reflect an increased gas density. The latter can be caused by major galaxy mergers (e.g., Narayanan et al. 2008; Juneau et al. 2009), which are common for high-redshift IR-selected galaxies above the sSFR sequence (Kartaltepe et al. 2012) and which are postulated to result in an increased star formation efficiency (Daddi et al. 2010) due to the "compacting" of the SF gas into a dense central starburst. Recent observations showed a correlation between AGN X-ray absorption and $\sim$100 pc scale starburst in nearby Seyferts (Diamond-Stanic & Rieke 2012), which can be broadly consistent with either of the above scenarios (torus-host galaxy link, or obscuration by $\sim$100 pc scale gas). Some simulations predict a multi-scale connection where the BH fueling (Hopkins & Quataert 2010) and/or torus properties (Hopkins et al. 2012) are related to the nuclear SFR via gas inflow albeit in a complicated and perhaps stochastic way. These possibilities are both very interesting as they differ from the typical AGN unified models where the very central region is assumed to be somewhat decoupled from its large-scale surroundings.

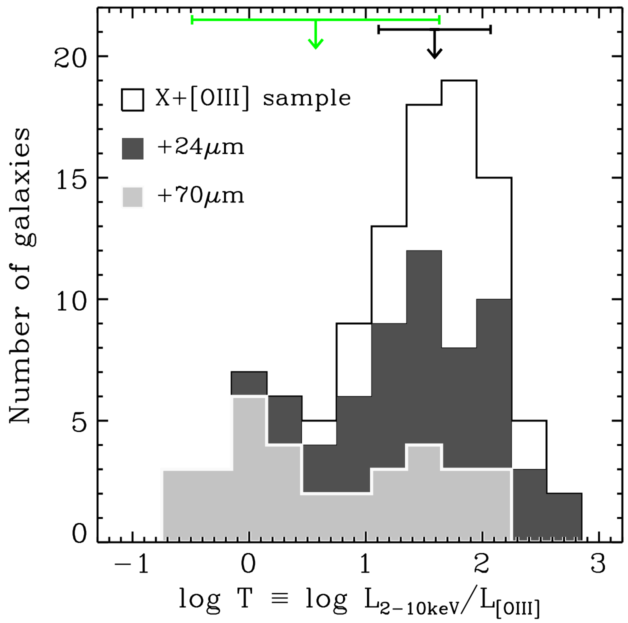

Figure 14. Distribution of the Compton-thickness parameter $T \equiv L_{2-10\,{\rm keV}}/L_{\rm [O\,III]\,\lambda 5007}$ for an X-ray + [O III]-selected sample of AGNs (black line). The distributions for the subsamples of galaxies detected at 24 μm and at 70 μm are overplotted in dark and light gray, respectively. The most absorbed systems (with lower values of T) are preferentially detected at 70 μm. This subsample displays a much broader distribution of thickness parameter and a larger relative number of absorbed AGNs compared to both the 24 μm sample and the parent X-ray + [O III]-selected sample. The arrows at the top of the figure indicate the mean and standard deviation for nearby AGNs that are either obscured, Type 2 (0.59 ± 1.06 dex; in green) or unobscured, Type 1 (1.59 ± 0.48 dex; in black; Heckman et al. 2005).

(A color version of this figure is available in the online journal.)

Complementary findings suggest that host-scale obscuration may hinder the detection of optical lines in hard X-ray-selected but optically dull AGNs (e.g., Rigby et al. 2006). These tend to reside in disky edge-on hosts and, if all optical signatures are lost, would be missed with the MEx diagnostic diagram. The host obscuration that we find here must have a smaller covering fraction of the NLRs in order to detect optical nebular line signatures in many cases.

---

[37] Although recent observations suggest some (at least small degree) alignment of AGN and their host galaxies (Lagos et al. 2011).

[38] We set $P({\rm AGN}) = 1$ if the source is selected as an X-ray AGN.

6.3. Properties of Absorbed and X-unabsorbed AGNs: An Evolutionary Sequence?

The stellar mass distributions of the weak and absorbed AGN samples are similar to one another, while the mass distribution of X-ray AGN is skewed toward higher stellar masses. According to Figure 3(a), the secure X-ray AGNs all have a high stellar mass $M_\star > 10^{10.6}\ M_\odot$, and seem to be more massive on average than the global AGN population. This suggests that X-ray-selected AGNs will tend to be more easily identified in more massive hosts. However, the statistics are poor with only 12 X-ray AGNs on the MEx diagram. Using a larger sample, Mullaney et al. (2012) found that X-ray-selected AGNs always lie in high stellar mass hosts ($\langle M_\star \rangle = 10^{10.7}$–$10^{10.8}\ M_\odot$) across a broad range of redshift (up to $z \sim 3$). This may be due to the presence of more massive BHs in these systems although the authors only found a weak correlation between stellar mass and X-ray luminosity over the 10^{42}–10^{44} erg s^{-1} range ($M_\star \propto L_X^{(1/7)}$). Aird et al. (2012) explain this feature with observational bias such that more massive BHs are observable at a broader range of Eddington ratios than less massive ones, which presumably reside in less massive hosts. While this selection bias will be especially true for X-ray selection, it is less severe with optical AGN diagnostics, which are sensitive down to much lower accretion rates. This may explain why the MEx method uncovers AGN down to lower stellar masses than the less sensitive X-ray method. However, every AGN selection is incomplete. Thus, it is of great interest to combine multi-wavelength indicators for the sake of completeness.

Relative to X-unabsorbed AGNs, the absorbed AGNs have similar bolometric luminosities but somewhat smaller stellar masses (and possibly smaller mass BHs). The absorbed AGN hosts are thus growing both their BHs and their stellar content *faster* (as they tend to have higher sSFR), in agreement with the results from Tanaka (2012). This is unlikely to result from an artifact due to [O III] being strongly contaminated by star formation because the [O III]-to-IR ratio is elevated in a similar fashion in both the absorbed and X-unabsorbed AGN hosts (right panel of Figure 5).

Those systematic differences between the absorbed and unabsorbed AGN hosts may correspond to an evolutionary sequence where absorbed AGNs tend to occur at the beginning of a growth cycle with higher specific growth rate and elusive X-ray signatures due to gaseous surroundings (on possibly a range of physical scales). X-ray unabsorbed AGNs would then correspond to more mature systems (consistent with higher stellar masses of the hosts) after some of the gas responsible for fueling and/or obscuring the central region has been consumed, pushed aside, or removed. This idea is similar to the well-known major merger scenario (Sanders et al. 1988; described in more detail in the next section), but could be more generic and also apply to AGNs with intermediate luminosities in isolated but initially gas-rich galaxies, assuming that even in those isolated systems the obscuring material could be gradually removed by the AGN and/or star formation. The less extreme AGN luminosities compared to the quasar regime mean that major galaxy mergers may not be required in all cases.

6.4. Physical Origin of High AGN Fractions

This study finds a larger AGN fraction (37%) among IR-luminous, SF galaxies than previous studies. Combining multi-wavelength diagnostics from X-ray to radio, Kartaltepe et al. (2010a) found that the AGN fraction rises steeply with IR luminosity and/or redshift (see the filled black circles in the left panel of Figure 6), but their values are lower than ours with an overall fraction ∼10%–20% over the redshift and luminosity ranges of interest in this paper. Similarly, Symeonidis et al. (2010) studied the occurrence of AGN in 70 μm galaxies over a similar redshift range and found an AGN fraction ∼13%. The main difference between these previous investigations and the current work is the use of the MEx diagnostic diagram, which unveils the majority of the AGNs including absorbed and weak systems. Some absorbed AGNs were successfully selected by previous authors with, e.g., mid-IR color diagnostics, but the latter are not as sensitive to the presence of active nuclei as the MEx method and are therefore less complete.

What are the physical causes of such a frequent occurrence of AGN? Is there a connection between AGN triggering and the elevated SFR in their host galaxies? Or between AGN absorption and their host galaxies? The results from this work imply that active SMBH growth occurs in parallel with active star formation. The elevated SFRs are probed by the FIR emission and there is a connection between the infrared luminosity and the occurrence of AGN. One interpretation that fits all of these observational trends is the major merger scenario (e.g., Sanders et al. 1988). Major mergers of gas-rich galaxies are expected to fuel both starbursts and AGN, with the AGN originally deeply buried in large amounts of gas before emerging as an X-ray-detected AGN. Qualitatively, our observations fit a merger scenario with simultaneous star formation and AGN activity. In contrast, several authors have pointed out that the morphologies of X-ray AGNs do not appear to be mergers more often than non-X-ray AGNs (Cisternas et al. 2011; Schawinski et al. 2011; Mullaney et al. 2012; Kocevski et al. 2012). However, these studies did not include the X-ray absorbed systems identified by the MEx method: it is possible that the X-ray-selected AGNs are not associated with mergers (or that they represent a different evolutionary stage) while the more absorbed AGNs are more directly triggered by mergers.

An interesting feature from this work is that the rise of the global AGN fraction with $L_{\rm IR}$ behaves similarly to the rise in the fraction of galaxies undergoing mergers and interactions and/or having an irregular morphology at $z \sim 1$ (dashed and dotted lines in Figure 6, taken from Kartaltepe et al. 2012).[39] In contrast, the fraction of X-ray unabsorbed AGNs is much lower and does not track well with the fraction of mergers and/or irregular galaxies. While somewhat indirect, this argument suggests that X-ray selection of AGN may miss the connection between AGN occurrence and galaxy interactions because of a possible mismatch between the timescale of AGN X-ray observability of the visibility timescale of mergers. Future studies of the connection between AGNs and their host galaxies should include both absorbed and unabsorbed AGNs to provide us with a more conclusive test.

Despite the apparent consistency of a merger picture, major galaxy mergers may not be required to explain our results. For instance, an alternative way to obtain a high incidence of AGNs and also a high incidence of AGN absorption could be large-scale disk instabilities in gas-rich SF galaxies, as exemplified by high-redshift clumpy galaxies (Elmegreen et al. 2007). These systems are more common at higher redshift ($z \gtrsim 2$) and may be explained by simulations (Agertz et al. 2009) in the context

---

[39] These fractions were calculated in a slightly different redshift range ($0.8 < z < 1.2$ rather than $0.3 < z < 1$) but are similar to what is expected at lower redshifts (Kartaltepe et al. 2010b) and so should not be significantly different at the exact redshift range of interest here.

of cold stream accretion cosmological models (e.g., Dekel et al. 2009). Clumpy galaxies persist down to intermediate redshift in intermediate-mass galaxies (Elmegreen et al. 2009). Unstable (or clumpy) disk galaxies are predicted (Bournaud et al. 2011) and observed (Bournaud et al. 2012) to efficiently fuel AGNs, including a high likelihood of absorption of X-ray signatures.

Irrespectively of the morphology and kinematics of the host galaxies, work by Tanaka (2012) on weak AGNs suggests that, like stronger AGNs, they occur predominantly in massive hosts ($>10^{10}\ M_\odot$). Those authors argued that the stellar mass of the host galaxies appears to act as a "switch" in triggering AGNs, but the underlying mechanism remains unknown given that they do not find dependencies on galaxy morphology. The weak AGNs from this paper would also be consistent with a "switch" at $\sim 10^{10}\ M_\odot$ but we do not probe to sufficiently low masses to really characterize that feature. Furthermore, the MEx diagram was designed with SDSS priors and so will only be sensitive to the stellar mass range over which the bulk of low-redshift SDSS AGNs can be identified with the traditional BPT diagrams.

While we cannot distinguish between major galaxy mergers, large-scale violent disk instabilities or other triggering mechanism without additional observations, it is clear that a complete picture of the growth of galaxies and their central SMBHs must include a gas-rich phase with concurrent SF and AGN, where the central AGN is often absorbed even for moderate-luminosity AGN ($10^{43.4} < L_{\rm bol}({\rm AGN}) < 10^{45}$ erg s^{-1}, i.e., below the quasar regime).

Lastly, while the AGN *fraction* of the intermediate-redshift FIR-selected sample is similar to that in nearby FIR-selected galaxies, the *number* of IR-luminous galaxies is much larger at higher redshift. This implies that the global AGN fraction in SF galaxies was higher in the past. A greater availability of gas at earlier epochs may be responsible for the more common occurrence of highly SF (thus IR-bright) galaxies. The high fraction of AGN, even if consistent with that at low redshift, implies that a much larger population of AGN—and especially X-ray absorbed AGN—in IR-luminous hosts exists at higher redshift. We may be starting to uncover the missing AGN population that has been inferred from cosmic X-ray background studies (Comastri et al. 1995; Mushotzky et al. 2000; Alexander et al. 2003; Bauer et al. 2004; Gilli et al. 2007).

7. SUMMARY

In this paper, we investigated the incidence of AGN among SF galaxies at intermediate redshift ($0.3 < z < 1$). The AGN fraction and AGN characteristics (X-ray unabsorbed, X-ray absorbed, intrinsically weak) are function of host galaxy properties. AGNs were identified based on four diagnostics: MEx diagram (Juneau et al. 2011), X-ray criteria (similar to Bauer et al. 2004), IRAC color–color (Stern et al. 2005), or IRAC [3.6]–[8.0] color versus redshift (Section 4.3). The last two are similar but not identical. Our main findings are as follows.

1. Combining all AGN diagnostics, the global AGN fraction is 37%(30%) ± 3% in the 70 μm selected galaxy population including (excluding) AGNs less luminous than $L_X = 10^{42}$ erg s^{-1} ($L_{\rm bol} = 10^{43.4}$ erg s^{-1}). This AGN fraction is around a factor of two greater than previous results in similar infrared luminosity and redshift ranges.
2. The fraction of SF galaxies hosting an AGN increases as a function of $L_{\rm IR}$. The AGN fractions are very similar to those in nearby ($0.05 < z < 0.1$) FIR-selected galaxies suggesting mild or no evolution since $z = 1$.
3. The differences between the higher fraction presented here relative to previous studies at comparable redshifts may be accounted for by (a) heavily absorbed AGNs and (b) intrinsically weaker AGNs. Absorbed and/or weak systems are more difficult to detect but can be identified thanks to the high sensitivity of the MEx diagnostic.
4. The fraction of galaxies hosting an AGN appears to be independent of the sSFR of the host, and remains elevated both on the sSFR sequence and above. In contrast, the fraction of AGNs that are X-ray absorbed increases substantially with increasing sSFR, possibly due to an increased gas fraction or gas density of the main/central SF regions in the host galaxies.
5. AGNs with the most X-ray absorption ($N_{\rm H} > 10^{24}$ cm^{-2}; inferred from $\log(L_X/L_{\rm [O\,III]}) < 0.3$) tend to reside in IR-luminous galaxies (detected at 70 μm). Adding less IR-luminous AGN host samples (undetected at 70 μm) mostly contributes unabsorbed and mildly absorbed AGNs (Section 6.2). Together with item 4, this result suggests a connection between the host galaxy's gas content and absorption of the central engine, which can be achieved either through absorption of the AGN X-rays by the ISM of the host galaxy or by a physical, multi-scale link between the host galaxy's gas content and the obscuring torus.
6. AGN radiation is likely responsible for the highest 24-to-70 μm flux ratios in the most extreme cases, which tend to be X-ray and optically selected AGNs. However, other factors must be at work to explain the spread of the mid- to far-IR color among SF galaxies and galaxies with a weak or absorbed AGN.

The authors acknowledge useful discussions with James Aird and a helpful report from the anonymous referee. The authors deeply thank the many members of the GOODS and AEGIS teams who obtained, reduced, and cataloged most of the data used in this paper.

This work is based in part on observations made with the *Spitzer Space Telescope*, which is operated by the Jet Propulsion Laboratory, California Institute of Technology under a contract with NASA, and on observations made with the *Chandra X-Ray Observatory*, operated by the Smithsonian Astrophysical Observatory for and on behalf of NASA under contract NAS8-03060. Additionally, some of the data used herein were obtained at the W. M. Keck Observatory, which is operated as a scientific partnership among the California Institute of Technology, the University of California, and the National Aeronautics and Space Administration. The Observatory was made possible by the generous financial support of the W. M. Keck Foundation. The Keck Observatory acknowledges the very significant cultural role and reverence that the summit of Mauna Kea has always had within the indigenous Hawaiian community and appreciate the opportunity to conduct observations from this mountain.

Funding for the DEEP2 survey has been provided by NSF grants AST95-09298, AST-0071048, AST-0071198, AST-0507428, and AST-0507483 as well as NASA LTSA grant NNG04GC89G. The analysis pipeline used to reduce the DEIMOS data was developed at UC Berkeley with support from NSF grant AST-0071048. The TKRS was funded by a grant to WMKO by the National Science Foundation's Small Grant for Exploratory Research program.

S.J. was partially funded by a FQRNT fellowship (Fonds Québécois de recherche sur la nature et la technologie, Canada),

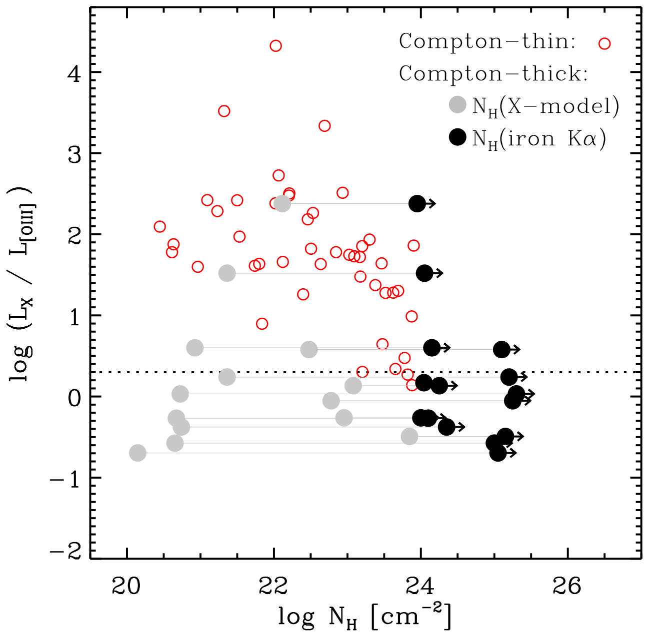

Figure 15. Compton-thickness parameter, L_X(2–10 keV)/L([O III] λ5007), as a function of X-ray absorption column density, $N_{\rm H}$, for nearby galaxies in the sample from B99. The column densities were derived by modeling the photoelectric cutoff in X-ray observations of Compton-thin (open circles) and Compton-thick (filled gray circles) AGNs. For the latter, a lower limit to $N_{\rm H}$ is also provided from the presence of Fe Kα line with substantial equivalent width (filled black circles; B99) and/or observations at energies beyond 10 keV. The two estimates of $N_{\rm H}$ for a given AGN are linked with thin solid lines. The dotted line marks the adopted threshold for heavy X-ray absorption. Points with $N_{\rm H}$ lower limits (of $N_{\rm H} = 10^{24}$ or $N_{\rm H} = 10^{25}$ cm^{-2}) are shifted slightly horizontally with respect to one another for clarity of the plotting symbols.

(A color version of this figure is available in the online journal.)

a Philanthropic Educational Organization (P.E.O.) Scholar Award. S.J. and F.B. acknowledge support from the EU through grants ERC-StG-257720 and CosmoComp ITN. J.R.M. thanks The Leverhulme Trust.

Facilities: Spitzer (MIPS, IRAC), Keck:II (DEIMOS), HST (ACS), CXO (ACIS), VLA

APPENDIX

AGN X-RAY ABSORPTION

This paper uses the Compton-thickness parameter as a proxy for AGN X-ray absorption (Sections 5.2 and 5.5). While this approach may not yield accurate measurements of the absorbing column density ($N_{\rm H}$), it allows us to separate the most heavily absorbed cases from the rest of the AGN population (X-ray unabsorbed and mildly absorbed). We demonstrate this with the analysis of nearby AGNs presented by Bassani et al. (1999, hereafter B99). The B99 sample is not statistically complete but it spans a broad range of X-ray absorption properties and includes measurements of [O III] λ5007 and 2–10 keV fluxes, iron Kα equivalent widths, and $N_{\rm H}$ from fitting the X-ray observations with a photoelectric cutoff model (assuming no components from reflection or stellar emission). In some cases, the authors note Compton-thick signatures with $N_{\rm H} > 10^{25}$ cm^{-2} if there is also absorption of X-rays at energies above 10 keV, or with $N_{\rm H} > 10^{24}$ cm^{-2} if there is no data available beyond 10 keV to rule out an absorbing column between 10^{24} cm^{-2} and 10^{25} cm^{-2} (see their Table 2).

As shown in Figure 15, the hard X-ray (2–10 keV) to [O III] λ5007 luminosity ratio drops when Compton thickness is reached at $N_{\rm H} \approx 10^{24}$ cm^{-2} (filled black circles). However, the most heavily absorbed systems can be mistaken for low-column density cases with simple X-ray spectra models that do not account for additional signatures such as the equivalent width of the Fe Kα emission line (which becomes high in cases of heavy absorption) or the absorption of even higher energy photons (>10 keV). This feature is obvious in Figure 15 where the two estimates of $N_{\rm H}$ for Compton-thick AGNs (see B99 for details on $N_{\rm H}$ calculations) can differ by 5 dex and typically by 3 dex. This shows the failure of the photoelectric cutoff estimate of $N_{\rm H}$ in cases of the heaviest absorption.

The Compton-thickness parameter tends to be low for the most absorbed systems. We adopted the threshold $\log(L_X/L_{\rm [O\,III]}) < 0.3$ dex to classify two AGNs that met the X-ray AGN criteria as X-absorbed AGNs rather than X-unabsorbed AGNs (Section 5.2 and Table 1). However, it is possible that other AGNs in the X-unabsorbed category have in fact significant absorption as we do not use X-ray spectral signatures due to the low number of X-ray counts (and associated uncertainties) for AGNs in our sample. In that sense, the absorbed fraction is a conservative lower limit and could be even higher if we moved more AGNs from the X-unabsorbed to the X-absorbed category.

In order to facilitate the comparison with the sample of interest in this work, we used the [O III] λ5007 fluxes uncorrected for dust obscuration. Applying the correction from the Balmer decrement method, as done by B99, would increase the [O III] λ5007 fluxes by 1.6 (1.0) dex on average (median) with some cases presenting more extreme obscuration (up to 2.7 dex). In particular, two of the three Compton-thick AGNs with $\log(L_X/L_{\rm [O\,III]}) > 0.3$ dex have extreme Balmer decrement values (>10), which implies that the observed [O III] λ5007 line is underluminous and leads to a higher Compton-thickness parameter.

REFERENCES

Abazajian, K. N., Adelman-McCarthy, J. K., Agüeros, M. A., et al. 2009, ApJS, 182, 543
Agertz, O., Teyssier, R., & Moore, B. 2009, MNRAS, 397, L64
Aird, J., Coil, A. L., Moustakas, J., et al. 2012, ApJ, 746, 90
Alexander, D. M., Bauer, F. E., Brandt, W. N., et al. 2003, AJ, 126, 539
Alexander, D. M., Bauer, F. E., Chapman, S. C., et al. 2005, ApJ, 632, 736
Alexander, D. M., & Hickox, R. C. 2012, NewAR, 56, 93
Barmby, P., Alonso-Herrero, A., Donley, J. L., et al. 2006, ApJ, 642, 126
Barmby, P., Huang, J.-S., Ashby, M. L. N., et al. 2008, ApJS, 177, 431
Bassani, L., Dadina, M., Maiolino, R., et al. 1999, ApJS, 121, 473
Bauer, F. E., Alexander, D. M., Brandt, W. N., et al. 2004, AJ, 128, 2048
Bournaud, F., Dekel, A., Teyssier, R., et al. 2011, ApJL, 741, L33
Bournaud, F., Juneau, S., Le Floc'h, E., et al. 2012, ApJ, 757, 81
Bourne, N., Dunne, L., Ivison, R. J., et al. 2011, MNRAS, 410, 1155
Brinchmann, J., Charlot, S., White, S. D. M., et al. 2004, MNRAS, 351, 1151
Bruzual, G., & Charlot, S. 2003, MNRAS, 344, 1000
Cameron, E. 2011, PASA, 28, 128
Chabrier, G. 2003, PASP, 115, 763
Chary, R., & Elbaz, D. 2001, ApJ, 556, 562
Cisternas, M., Jahnke, K., Inskip, K. J., et al. 2011, ApJ, 726, 57
Colbert, E. J. M., Heckman, T. M., Ptak, A. F., Strickland, D. K., & Weaver, K. A. 2004, ApJ, 602, 231
Comastri, A., Setti, G., Zamorani, G., & Hasinger, G. 1995, A&A, 296, 1
Condon, J. J. 1992, ARA&A, 30, 575
Cooper, M. C., Aird, J. A., Coil, A. L., et al. 2011, ApJS, 193, 14
Cooper, M. C., Newman, J. A., Davis, M., Finkbeiner, D. P., & Gerke, B. F. 2012, Astrophysics Source Code Library, 3003
Croton, D. J., Springel, V., White, S. D. M., et al. 2006, MNRAS, 365, 11
Daddi, E., Bournaud, F., Walter, F., et al. 2010, ApJ, 713, 686
Dale, D. A., & Helou, G. 2002, ApJ, 576, 159
Davis, M., Faber, S. M., Newman, J., et al. 2003, Proc. SPIE, 4834, 161
Davis, M., Guhathakurta, P., Konidaris, N. P., et al. 2007, ApJL, 660, L1

Dekel, A., Sari, R., & Ceverino, D. 2009, ApJ, 703, 785

Del Moro, A., Alexander, D. M., Mullaney, J. R., et al. 2013, A&A, 549A, 59

Diamond-Stanic, A. M., & Rieke, G. H. 2012, ApJ, 746, 168

Diamond-Stanic, A. M., Rieke, G. H., & Rigby, J. R. 2009, ApJ, 698, 623

Dickinson, M. IDEL team. 2007, BAAS, 38, 822

Di Matteo, T., Springel, V., & Hernquist, L. 2005, Natur, 433, 604

Donley, J. L., Koekemoer, A. M., Brusa, M., et al. 2012, ApJ, 748, 142

Donley, J. L., Rieke, G. H., Pérez-González, P. G., Rigby, J. R., & Alonso-Herrero, A. 2007, ApJ, 660, 167

Donley, J. L., Rieke, G. H., Rigby, J. R., & Pérez-González, P. G. 2005, ApJ, 634, 169

Elbaz, D., Daddi, E., Le Borgne, D., et al. 2007, A&A, 468, 33

Elbaz, D., Dickinson, M., Hwang, H. S., et al. 2011, A&A, 533A, 119

Elbaz, D., Hwang, H. S., Magnelli, B., et al. 2010, A&A, 518, L29

Elmegreen, D. M., Elmegreen, B. G., Marcus, M. T., et al. 2009, ApJ, 701, 306

Elmegreen, D. M., Elmegreen, B. G., Ravindranath, S., & Coe, D. A. 2007, ApJ, 658, 763

Elvis, M., Wilkes, B. J., McDowell, J. C., et al. 1994, ApJS, 95, 1

Fabbiano, G. 1989, ARA&A, 27, 87

Ferrarese, L., & Merritt, D. 2000, ApJL, 539, L9

Frayer, D. T., Fadda, D., Yan, L., et al. 2006, AJ, 131, 250

Gabor, J. M., Davé, R., Oppenheimer, B. D., & Finlator, K. 2011, MNRAS, 417, 2676

Gabor, J. M., Impey, C. D., Jahnke, K., et al. 2009, ApJ, 691, 705

Gilli, R., Comastri, A., & Hasinger, G. 2007, A&A, 463, 79

Hatziminaoglou, E., Omont, A., Stevens, J. A., et al. 2010, A&A, 518, L33

Heckman, T. M., Ptak, A., Hornschemeier, A., & Kauffmann, G. 2005, ApJ, 634, 161

Hickox, R. C., Jones, C., Forman, W. R., et al. 2009, ApJ, 696, 891

Ho, L. C. 2008, ARA&A, 46, 475

Hopkins, P. F., Hayward, C. C., Narayanan, D., & Hernquist, L. 2012, MNRAS, 420, 320

Hopkins, P. F., Hernquist, L., Cox, T. J., et al. 2006, ApJS, 163, 1

Hopkins, P. F., & Quataert, E. 2010, MNRAS, 407, 1529

Hwang, H. S., Elbaz, D., Lee, J. C., et al. 2010a, A&A, 522, A33

Hwang, H. S., Elbaz, D., Magdis, G., et al. 2010b, MNRAS, 409, 75

Ivison, R. J., Chapman, S. C., Faber, S. M., et al. 2007, ApJL, 660, L77

Jahnke, K., & Macciò, A. V. 2011, ApJ, 734, 92

Juneau, S., Dickinson, M., Alexander, D. M., & Salim, S. 2011, ApJ, 736, 104

Juneau, S., Narayanan, D. T., Moustakas, J., et al. 2009, ApJ, 707, 1217

Kartaltepe, J. S., Dickinson, M., Alexander, D. M., et al. 2012, ApJ, 757, 23

Kartaltepe, J. S., Sanders, D. B., Le Floc'h, E., et al. 2010a, ApJ, 709, 572

Kartaltepe, J. S., Sanders, D. B., Le Floc'h, E., et al. 2010b, ApJ, 721, 98

Kauffmann, G., Heckman, T. M., Tremonti, C., et al. 2003, MNRAS, 346, 1055

Kennicutt, R. C., Jr. 1998, ARA&A, 36, 189

Kewley, L. J., Groves, B., Kauffmann, G., & Heckman, T. 2006, MNRAS, 372, 961

Kewley, L. J., Heisler, C. A., Dopita, M. A., & Lumsden, S. 2001, ApJS, 132, 37

Kocevski, D. D., Faber, S. M., Mozena, M., et al. 2012, ApJ, 744, 148

Lacy, M., Storrie-Lombardi, L. J., Sajina, A., et al. 2004, ApJS, 154, 166

La Franca, F., Fiore, F., Comastri, A., et al. 2005, ApJ, 635, 864

Lagos, C. D. P., Padilla, N. D., Strauss, M. A., Cora, S. A., & Hao, L. 2011, MNRAS, 414, 2148

Laird, E. S., Nandra, K., Georgakakis, A., et al. 2009, ApJS, 180, 102

Le Floc'h, E., Papovich, C., Dole, H., et al. 2005, ApJ, 632, 169

Lutz, D., Mainieri, V., Rafferty, D., et al. 2010, ApJ, 712, 1287

Magdis, G. E., Daddi, E., Béthermin, M., et al. 2012, ApJ, 760, 6

Magnelli, B., Elbaz, D., Chary, R. R., et al. 2009, A&A, 496, 57

Magnelli, B., Elbaz, D., Chary, R. R., et al. 2011, A&A, 528, A35

Magorrian, J., Tremaine, S., Richstone, D., et al. 1998, AJ, 115, 2285

Mannucci, F., Cresci, G., Maiolino, R., Marconi, A., & Gnerucci, A. 2010, MNRAS, 408, 2115

Maoz, D. 2007, MNRAS, 377, 1696

Marcillac, D., Elbaz, D., Chary, R. R., et al. 2006, A&A, 451, 57

Marconi, A., Risaliti, G., Gilli, R., et al. 2004, MNRAS, 351, 169

Merloni, A. 2004, MNRAS, 353, 1035

Morrison, G. E., Owen, F. N., Dickinson, M., Ivison, R. J., & Ibar, E. 2010, ApJS, 188, 178

Mulchaey, J. S., Koratkar, A., Ward, M. J., et al. 1994, ApJ, 436, 586

Mullaney, J. R., Alexander, D. M., Goulding, A. D., & Hickox, R. C. 2011, MNRAS, 414, 1082

Mullaney, J. R., Alexander, D. M., Huynh, M., Goulding, A. D., & Frayer, D. 2010, MNRAS, 401, 995

Mullaney, J. R., Pannella, M., Daddi, E., et al. 2012, MNRAS, 419, 95

Mushotzky, R. F., Cowie, L. L., Barger, A. J., & Arnaud, K. A. 2000, Natur, 404, 459

Nandra, K., Laird, E. S., Adelberger, K., et al. 2005, MNRAS, 356, 568

Narayanan, D., Cox, T. J., Shirley, Y., et al. 2008, ApJ, 684, 996

Newman, J. A., Cooper, M. C., Davis, M., et al. 2012, arXiv:1203.3192

Noeske, K. G., Weiner, B. J., Faber, S. M., et al. 2007, ApJL, 660, L43

Ptak, A., Yaqoob, T., Mushotzky, R., Serlemitsos, P., & Griffiths, R. 1998, ApJL, 501, L37

Rieke, G. H., Alonso-Herrero, A., Weiner, B. J., et al. 2009, ApJ, 692, 556

Rigby, J. R., Rieke, G. H., Donley, J. L., Alonso-Herrero, A., & Pérez-González, P. G. 2006, ApJ, 645, 115

Rodighiero, G., Daddi, E., Baronchelli, I., et al. 2011, ApJL, 739, L40

Rosario, D. J., Santini, P., Lutz, D., et al. 2012, A&A, 545, A45

Roy, A. L., & Norris, R. P. 1997, MNRAS, 289, 824

Rujopakarn, W., Rieke, G. H., Eisenstein, D. J., & Juneau, S. 2011, ApJ, 726, 93

Salpeter, E. E. 1955, ApJ, 121, 161

Sanders, D. B., Soifer, B. T., Elias, J. H., et al. 1988, ApJ, 325, 74

Sargent, M. T., Béthermin, M., Daddi, E., & Elbaz, D. 2012, ApJL, 747, L31

Sargent, M. T., Schinnerer, E., Murphy, E., et al. 2010, ApJS, 186, 341

Savaglio, S., Glazebrook, K., Le Borgne, D., et al. 2005, ApJ, 635, 260

Schawinski, K., Treister, E., Urry, C. M., et al. 2011, ApJL, 727, L31

Shao, L., Lutz, D., Nordon, R., et al. 2010, A&A, 518, L26

Smith, D. J. B., Dunne, L., da Cunha, E., et al. 2012, MNRAS, 427, 703

Stern, D., Eisenhardt, P., Gorjian, V., et al. 2005, ApJ, 631, 163

Symeonidis, M., Rosario, D., Georgakakis, A., et al. 2010, MNRAS, 403, 1474

Tacconi, L. J., Genzel, R., Neri, R., et al. 2010, Natur, 463, 781

Tanaka, M. 2012, PASJ, 64, 37

Tremaine, S., Gebhardt, K., Bender, R., et al. 2002, ApJ, 574, 740

Tremonti, C. A., Heckman, T. M., Kauffmann, G., et al. 2004, ApJ, 613, 898

Trouille, L., Barger, A. J., & Tremonti, C. 2011, ApJ, 742, 46

Trump, J. R., Impey, C. D., Kelly, B. C., et al. 2009, ApJ, 700, 49

Trump, J. R., Impey, C. D., Kelly, B. C., et al. 2011, ApJ, 733, 60

Trump, J. R., Konidaris, N. P., Barro, G., et al. 2013, ApJL, 763, L6

Ueda, Y., Akiyama, M., Ohta, K., & Miyaji, T. 2003, ApJ, 598, 886

Vasudevan, R. V., & Fabian, A. C. 2007, MNRAS, 381, 1235

Vasudevan, R. V., & Fabian, A. C. 2009, MNRAS, 392, 1124

Veilleux, S., Kim, D.-C., & Sanders, D. B. 2002, ApJS, 143, 315

Wirth, G. D., Willmer, C. N. A., Amico, P., et al. 2004, AJ, 127, 3121

Yan, R., Ho, L. C., Newman, J. A., et al. 2011, ApJ, 728, 38

Yan, R., Newman, J. A., Faber, S. M., et al. 2006, ApJ, 648, 281

Yuan, T., Kewley, L. J., & Sanders, D. B. 2010, ApJ, 709, 884